COMPUTER SIMULATION, FABRICATION AND CHARACTERIZATION OF INVERSE FRUSTUM NANOSPHERE METAL ARRAYS FOR FIBER-BASED PLASMONIC SENSORS

by

JIAQI WU

Presented to the Faculty of the Graduate School of

The University of Texas at Arlington in Partial Fulfillment

of the Requirements

for the Degree of

MASTER OF SCIENCE IN MATERIALS SCIENCE AND ENGINEERING

THE UNIVERSITY OF TEXAS AT ARLINGTON

December 2012

ACKNOWLEDGEMENTS

First of all, I would like to thank my advisor, Dr. Yaowu Hao for his guidance, support, and encouragements, in both research and life. I would appreciate Dr. Digant Dave's co-advising as well. Without his fully support on optical knowledge and optical measurements, this thesis cannot be done.

Second, I would like to thank Dr. Fuqiang Liu and Dr. Seong Jin Koh for serving in my thesis committee. I learned a lot from them in both research and courses. I also want to show my gratitude to James Nyagilo in Dr. Dave's group, his strong research ability and insightful suggestions helped a lot in this project. Besides, I am so happy that I have many great lab mates around me. Mark, Kevin, Alex, Ivan, Koi and Mook, without their advice and help, this thesis can never be done. Third, I would like to thank CCMB and NanoFab for providing state of art facilities for my research.

At last, I would like to thank my parents and my girl friend, who have given everything they have to encourage me, inspire me towards the success I have achieved so far.

Nov. 20th, 2012

ABSTRACT

COMPUTER SIMULATION, FABRICATION AND CHARACTERZTION OF INVERSE FRUSTUM NANOSPHERE METAL ARRAYS FOR FIBER-BASED PLASMONIC SENSORS

Jiaqi Wu, M.S.

The University of Texas at Arlington, 2012

Supervising Professor: Yaowu Hao

In recent years, a number of metal nanostructures have attracted huge attention from scientists and researchers for its plasmonic property and surface enhanced Raman scattering effect. They have been utilized to monitor molecule adsorption, antibody-antigen reorganization event, and to enhance scattering for identification of molecules even in very low concentration. They both have also been exploited for real time biosensing.

In this thesis, we are investigating a new plasmonic structure, inverse frustum nanosphere gold arrays, and exploring its optical fiber-based sensing application. The nanostructure was fabricated by electro-deposition of gold into pre-assembled templates, which are made of monodispered colloidal polystyrene nanospheres in a hexagonal close packing structure. The structure is further modified by introducing circular bottom hole to each hemispherical void for optical fiber-based probe application. Its plasmonic sensing behavior is demonstrated. The effect of structure parameters, such as gold film thickness and bottom hole diameter on LSPR is symmetrically studied in both experiments and simulations. The advantage

of this structure against lithographically patterned cylindrical hole arrays is displayed and its potential application as molecule adsorption monitor is predicted and tested.

TABLE OF CONTENTS

LIST OF ILLUSTRATIONS

CHAPTER 1

INTRODUCTION

In the past two decades, the field of plasmonics is rapidly becoming of interest to a broad range of disciplines.[1] Driven by the desire to develop plasmonic devices, plasmonics finds its application in various fields such as optical switching[2], near-field photonics[3] and surface enhanced Raman spectroscopy[4] based on surface plasmon resonance effect. Surface plasmons are electromagnetic waves coupled to electron cloud fluctuations, and are pinned to the metal/dielectric interface. When dimensions (at least one) of the metal is much smaller than the wavelength of the light, the collective excitation mode of the plasmons will be localized near the surface, and the resonant frequency will shift from the ordinary plasma frequency to Surface Plasmon Resonance (SPR) frequency. The incident light at SPR frequency is strongly absorbed and scattered; meantime the electric field associated with the incident light will be greatly enhanced. The extremely intense and highly confined electromagnetic fields induced by localized surface plasmon resonance (LSPR) can be utilized as a highly sensitive probe to detect small changes in the dielectric environment due to the biomolecular interactions at the surface. These changes can then be monitored via the LSPR peak wavelength shift. [5]This phenomenon provides a promising technique for sensing and identifying molecular species.

Optical fiber is an ideal platform for plasmonic sensing in remote locations and for small sample volume, offering the ability to probe solutions for in situ chemical sensing and in vivo biosensing. As nano-fabrication processes have rapidly developed, considerable number of fiber based plasmonic structures produced by different methods has been reported. These structures include nanochannels, nanotubes, nanodots, coated nanoparticles, etc. manufactured by sputtering, imprinting, chemistry synthesis and lithography. On these patterned surfaces, certain plasmon resonance frequency will be excited and the plasmonic modes will be ignited. However, fabrication of fiber probe which is cost-effective and able to produce reproducible results is really

a challenge. To date, high cost and poor reproducibility are two major issues they are suffering. Most importantly, the enhancement almost vanishes at even just 10nm away from the surface. Therefore, the sensing requires the analyte molecules bind or be in very close proximity to the surface. For detecting molecules in a solution, this fundamental limitation greatly reduces the sensitivity or/and lengthens the response time.

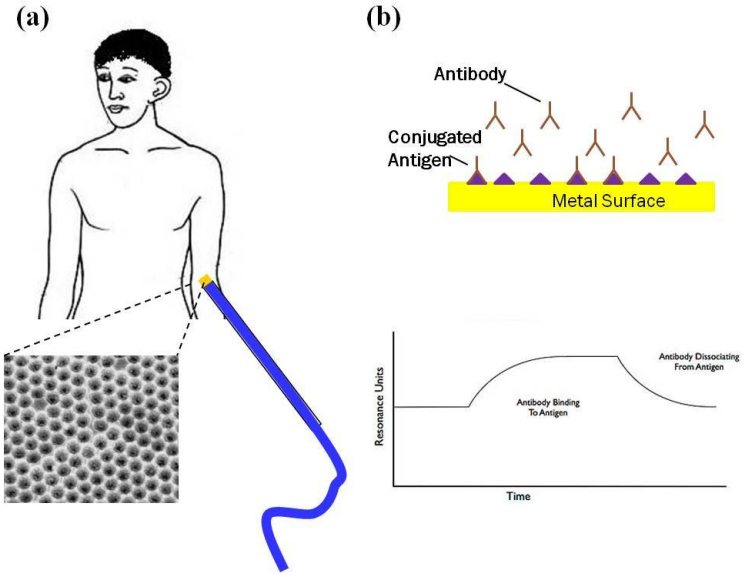

Figure 1-1 (a) In situ and en vivo fiber sensing probe with honeycomb structure on the tip (b) Monitoring of molecule adsorption on the tip surface

During the past few years, a series of publication has shown that continuous metal nanovoid arrays have the potential to be reproducible plasmonic substrates. With the commercialization of monodispersive colloidal nanospheres mainly polystyrene and silica, large crystal templates become easy to produce. By electroplating metals into self-assembled nanosphere crystal templates, an inverse replica of metal nanostructure can be created after the removal of the template. Such Ag and Au nanostructures with dimension within a couple of hundred nanometers yield unique SPR effect. Unlike other processes, this “lost wax” casting technique shows the potential to overcome the limitation and inconvenience to produce sensitive and reproducible plasmonic surface with high throughput and low cost. In this new structure, the voids, normally a couple of hundred nanometers in diameter are embedded in the film with the

thickness less than the void diameter. In addition, changing structure parameters such as void height and diameter has been very easy to make the localized plasmons tunable to achieve maximum surface plasmon resonance in visible and near infrared light spectrum. More importantly, due to the large size of the voids, effective distance is extended from 10nm to 100 nm away from the surface, which remarkably increases the volume of the plasmon-sensitive zone. In a word, this nanovoids array structure is highly worth of studying and an excellent candidate for fiber based sensor.

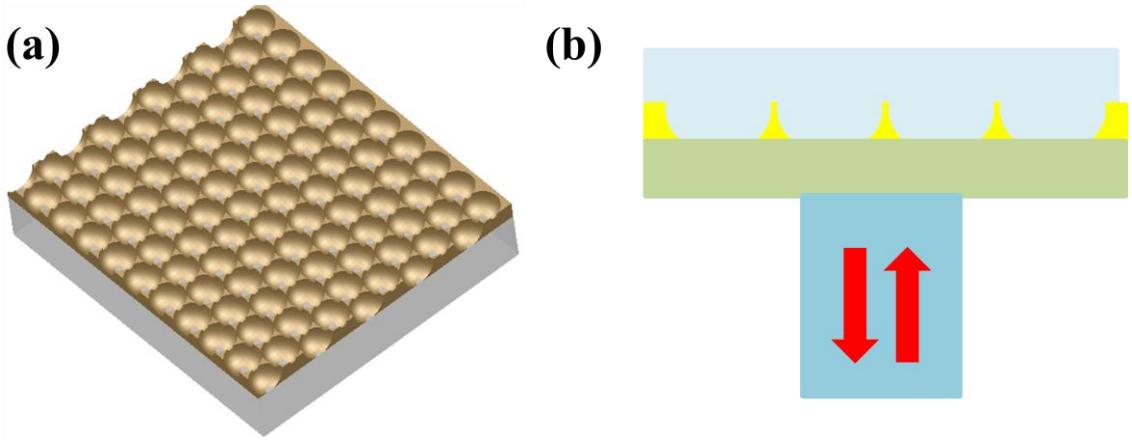

Figure 1-2 (a) 3D scheme of nanovoid structure (b) Its plasmonic sensing strucutre

In this study, polystyrene nanosphere self-assembly technique has been developed. Au electrochemical deposition has been performed using the template. Au nanovoid arrays for optical fiber tip have been fabricated, and their plasmonic properties and sensing behavior have been investigated and demonstrated through computer simulation and experiments.

CHAPTER 2

BACKGROUND INFORMATION

In this chapter, fundamentals of plasmonics, localized surface plasmon resonance (LSPR) and its applications as nano-scale bio-sensing are first introduced. Then, colloidal solution and self-assembly of colloidal crystals are described. At last, the simulation approach using Lumerical FDTD Solutions is introduced.

2.1 Plasmonics and Bio-sensing

Research in plasmonics is currently taking place at a breathtaking pace. It explores how electromagnetic fields can be confined over dimensions on the order of or smaller than the wavelength. It is based on interaction processes between electromagnetic radiation and conduction electrons at metallic interfaces or in smaller metallic nanostructures, leading to an enhanced electromagnetic near-field in small dimension. With years of efforts, it has given rise to a series of applications such as data transportation, decoration, spectroscopy and sensing. Among them, nanoscale biosensing for reading DNA bases [6] as well as detecting protein-protein interactions [7] , surface membrane binding events [8] and antigen-antibody recogniation events [9] has been paid most attention due to the advantage of label-free, low interference, and real-time monitoring [10]. When biomolecules bind at the surface of the plasmonic nanostructures, local refractive index changes. It can be monitored via the LSPR peak shift. To date, a large number of nanostructures have been fabricated and configured, towards larger detection range, higher sensitivity, lower cost and more stable performance.[11-13]

2.1.1 Fundamentals of Plasmonics and its Applications

In physics, a plasmon is a quasiparticle resulting from the quantization of plasma oscillation. It refers to the collective oscillation of the free electron gas in a piece of conductive material. When a metal cube is under the radiation of the light, in another word, exposed to a uniform electromagnetic field, the electrons will move in the opposite direction of the field leaving

positive ions on the other side. Once external field is turned off, the charge, both positive and negative, tends to move towards each other causing an “overshoot” due to the electrostatic force. As a result, the electrons will oscillate back and forth at a specific frequency, which is called plasma frequency, until the energy is lost in some kind of resistance or damping. Plasmons are a quantization of this kind of oscillation. Surface plasmons (SP) are those plasmons that are confined to the interface between a metal and a dielectric, they interact strongly with the light resulting in a polariton called surface plasmon plariton (SPP).

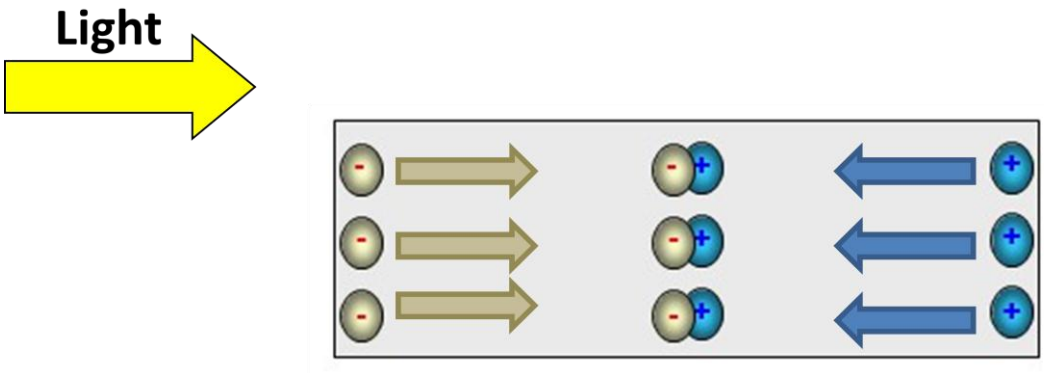

Figure 2-1 Scheme of plasma oscillation in a piece of metal induced by electromagnetic wave

Plasmons play a significant role in the optical properties of metals. Metals are highly reflective because their plasma frequency lies in the ultraviolet which is higher than the frequency of the visible light. As a result, the electrons in the metal screen the electric field of the light and the light is reflected making the metals shiny. In a typical reflection measurement of a plasmonic material, the incident light with certain wavelength will be coupled and adsorbed by the material that has the same SPR wavelength to excite SPP. As a result, an extinction peak will appear in the spectrum.

More recently, SP and SPP have the unique capacity to confine light to very small dimensions which could enable many new applications. Controlling of the surface feature, for instance, particles’ shape and size, enables the coupling and excitation of different SP modes. As a result, a vibrant color is given such as the historic stained glass which adorns medieval

cathedrals. SPP has been proposed as a means of super-resolution microscopy and photolithography due to their extremely small wavelength. In this case, the light is highly localized in a 2D geometry (mirrors, lenses, resonators etc.) to produce large-wave-vector (small wavelength) SPP for higher resolution imaging than conventional optical microscope, whose resolution is limited due to the diffraction of the light. The principal above also plays a role in surface enhanced Raman spectroscopy (SERS) which is a surface sensitive technique that enhances Raman scattering of the molecules adsorbed on rough metal surfaces due to the significant enhancement of the electric field. Furthermore, since position and intensity of plasmon absorption are highly affected by the surface property of the materials, it is often used by biochemists to study the mechanisms and kinetics of molecule adsorption and ligand-receptor binding events.

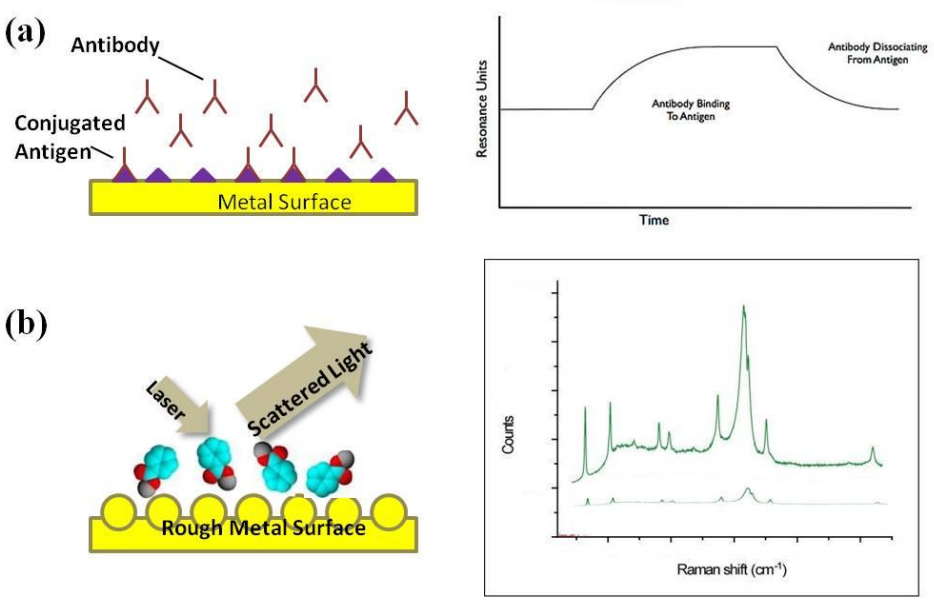

Figure 2-2 (a) Sketch of molecule adsorption behavior and its corresponding spectrum (b) Sketch of surface enhanced Raman scattering and corresponding spectrum

2.1.2 Principal of Localized Surface Plasmon Resonance (LSPR) and Nanostructures for Bio-sensing

Surface plasmon resonance (SPR) is the resonant, collective oscillation of valence electrons in a metal induced by incident light. The resonance condition is established when the

frequency/wave vector of the light photons matches the frequency/wave vector of surface plasmons. SPR in nano-scale structures is called LSPR. The LSPR phenomenon is theoretically possible in any kind of metal, semiconductor or alloy with a large negative real part and small imaginary part of electric permittivity.

We can obtain the explicit form of electromagnetic field distribution under some assumptions when a small particle is exposed to electromagnetic field. First, we assume that the particle size is much smaller than the wavelength of the light in the surrounding medium. Second, the particle is a homogeneous isotropic sphere with radius a, and surrounding material is a homogeneous, isotropic and non-absorbing medium. In static electric fields, Laplace equation for the potential $\nabla^2\phi = 0$ is solved. The solutions for this Laplace equation for potentials inside and outside the particle can be written as:

$$\phi_{in} = -\frac{3\varepsilon_m}{\varepsilon + 2\varepsilon_m} E_0 r\cos\theta \qquad (2\text{-}1)$$

$$\phi_{out} = -E_0 r\cos\theta + \frac{p}{4\pi\varepsilon_0\varepsilon_m r^2} \qquad (2\text{-}2)$$

where ε_m is the dielectric constant of medium; ε is the dielectric constant of the sphere; E_0 is the external field; r is the position vector at point P; a is the radius of the sphere; p is the dipole moment with the form:

$$p = 4\pi\varepsilon_0\varepsilon_m a^3 \frac{\varepsilon - \varepsilon_m}{\varepsilon + 2\varepsilon_m} E_0 \qquad (2\text{-}3)$$

If we introduce polarizability α via $p = \alpha\varepsilon_0\varepsilon_m E_0$, we can express α as:

$$\alpha = 4\pi a^3 \frac{\varepsilon - \varepsilon_m}{\varepsilon + 2\varepsilon_m} \qquad (2\text{-}4)$$

The equation above can be expanded in case of arbitrary shaped particles as:

$$\alpha = (1+\kappa)\varepsilon\Omega \frac{\varepsilon - \varepsilon_m}{\varepsilon + (1+\kappa)\varepsilon_m} \qquad (2\text{-}5)$$

where Ω is the volume of the particle. Dipolar polarizability α could be maximized at the condition $\mathrm{Re}[\varepsilon(\omega)] = -\kappa\varepsilon_m$, which is resulted from the resonance condition of LSPR assuming $\mathrm{Im}[\varepsilon(\omega)]$ is relatively small. κ is a shape factor that presents geometrical polarizability of the surface that indicates the electron oscillations. The shape factor of a small nanostructure plays a critical role to increase dipolar polarizability. This variable can be straightforwardly expressed by aspect ratio [14]. More needle-like are particles made such as nanorods, higher aspect ratio is achieved to linearly increase the resonant enhancement leading to sensitivity improvement accompanied by remarkable wavelength shift.

Surface plasmon plaritons (SPP) are electromagnetic excitations propagating at the interface between a dielectric and a conductor via the coupling of the light to surface plasmon. If the external charge and current are zero on the matter surface, the wave vector of the SP, K_{SP} on the plane surface, by solving Maxwell's equation with proper boundary conditions is equal to:

$$K_{SP} = \frac{2\pi}{\lambda}\sqrt{\frac{\varepsilon\varepsilon_m}{\varepsilon+\varepsilon_m}} \qquad (2\text{-}6)$$

According to Drude-Larentz model under low damping term, the resonance frequency of the surface plasmon $\varpi_{sp} = \frac{\varpi_p}{\sqrt{1+\varepsilon_m}}$, where $\varpi_p = \sqrt{\frac{ne^2}{\varepsilon_0 m}}$ is the plasma frequency of the metal. As a result, when $\varepsilon = -\varepsilon_m$, K_{SP} goes to infinity and the corresponding frequency approaches ϖ_{sp}.

On the other hand, the wave vector of the photons has the form of $\kappa = \frac{2\pi}{\lambda}$, which means the surface plasmon has greater momentum than that of a free space photon at the same frequency. Therefore, in order to excite the SPP, certain phase matching techniques have to be applied. There are certainly several methods available for exciting SPR, here, the two most common approaches, which are prism coupling and grating coupling, will be introduced. Later on, novel nano and mirco SPR active structures will be listed.

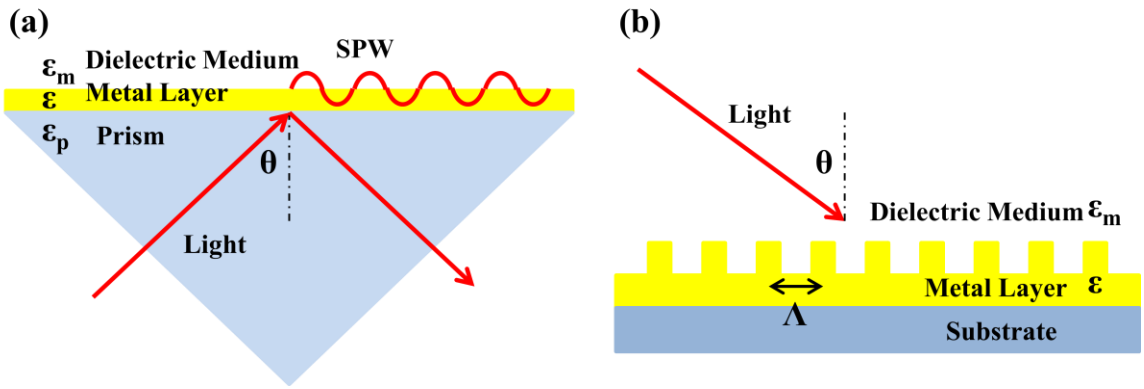

Figure 2-3 (a) Sketch of prism coupling method to excite SPW at metal/dielectric interface (b) Sketch of grating coupling with the a grating period of Λ

First, prism coupling is first utilized by Kretschmann in the attenuated total reflection method by means of a prism coupler. [15] A high refractive index prism with dielectric constant ε_p is coated with a thin metal film, and a semi-infinite dielectric, for simplicity air, is positioned outside it. When a light propagating in the prism is incident on the metal film with an angle larger than the critical angle, it will be reflected back into the prism. Evanescently decaying fields penetrate into the thin metal layer and remain at the other boundary (between metal and air). Under a phase matching condition, SPP is excited and it will propagate at the interface. Recalling the propagation constant of SPP

$$K_{SP} = \frac{2\pi}{\lambda}\sqrt{\frac{\varepsilon\varepsilon_m}{\varepsilon+\varepsilon_m}}, \qquad (2\text{-}7)$$

which is influenced by the presence of the dielectric on the other side of the metal film, the propagation constant of in-plane evanescent wave is given by

$$K_z = k\sqrt{\varepsilon_p}\sin\theta \qquad (2\text{-}8)$$

where θ and k are the incidence angle and wave vector of the light respectively. This way, SPP between the light lines of air and the prism can be excited. Note that phase matching to SPP at the prism/metal interface cannot be achieved, since the SPP dispersion lies outside the prism light cone. The SPP at the interface is also able to radiate light back into the metal film and the radiation destructively interferes with the reflected component of the incident light and hence,

leads to a reduction in the overall reflection. In an ideal case, the overall reflection becomes zero and the entire radiation field is converted to SPPs.

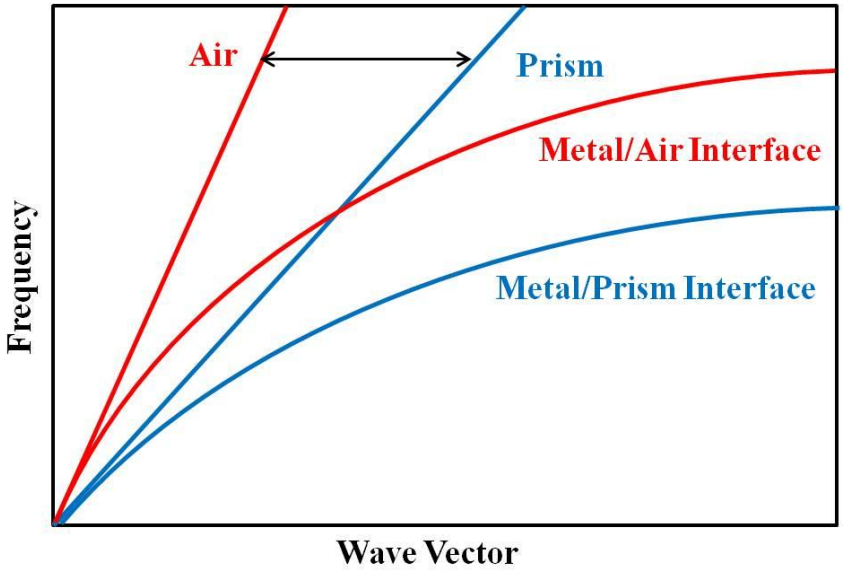

Figure 2-4 Dispersion relation of photons and surface plasmons at metal/air interface and metal/prism interface

Second, grating coupling [10] is also an effective method to overcome the mismatch in wave vector between the in-plane momentum of photons and SP by patterning the metal surface with a shallow grating of grooves or holes. For a simple one-dimensional grating, phase-matching takes place whenever the condition

$$K_{SP} = k\sin\theta + m\frac{2\pi}{\Lambda} \qquad (2\text{-}9)$$

is fulfilled, where m is an integer representing the diffraction order and Λ is the grating period. It is already a commercial product and it is the scheme of most plasmonic sensor. However, it only serves as a plasmonic substrate instead of a probe since analytical solution has to be placed on top of the metal layer where the incident light is illuminating at.

To date, there have been so many nanostructures designed and constructed for the excitation of LSPR and thus LSPR bio-sensor. LSPR offers a good and effective platform for biological and chemical sensing. [9] Specially, the differences of local refractive index, which is the square root of the dielectric constant, induced by biological interactions can be discerned

utilizing the exclusive properties of LSPR. Usually, organic molecules are employed to characterize the qualitative detection of bio-interaction due to its higher refractive index than buffer solution. When organic molecules bind to the metallic interface, the local refractive index increases accompanied with a red shift of the extinction spectrum. In a word, LSPR nano-sensors are good candidates for achieving fast, efficient detection of lipid membranes, protein binding and other interactions in native environments.

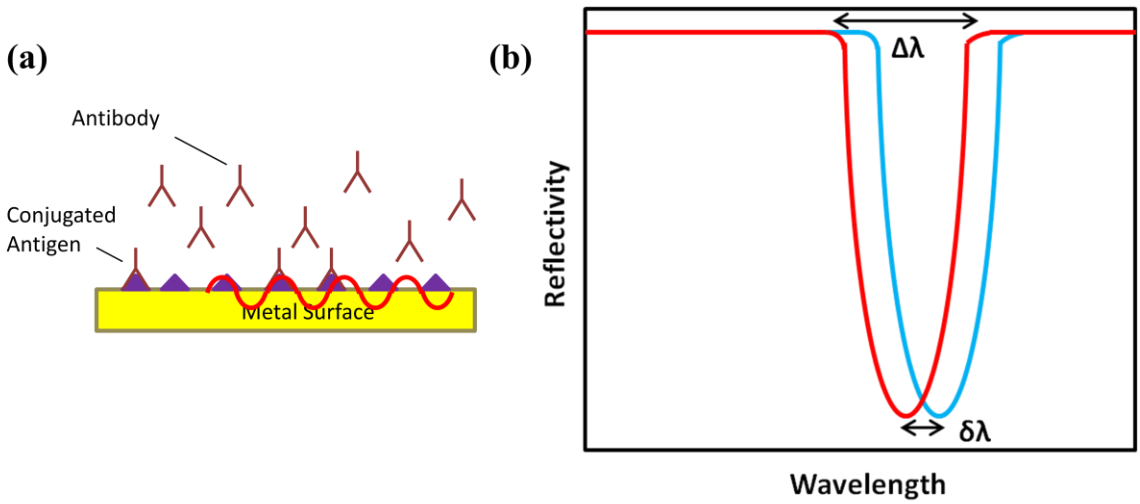

Figure 2-5 (a) Sketch of molecule adsorption on a metal surface (b) Resulting LSPR peak red shift in a reflectance spectrum

In order to compare sensing performance for LSPR nanostructures introduced later, several major factors such as sensitivity, figure of merit (FOM) and resolution will be introduced. First of all, sensitivity S is defined as the ratio of resonant wavelength shift $\delta\lambda_{res}$ to the variation of surrounding refractive index δn_s:

$$S = \frac{\delta\lambda res(nm)}{\delta ns(RIU)} \qquad (2\text{-}10)$$

where RIU means refractive index unit. FOM is considered as a useful parameter in evaluating LSPR nanosensor. It is defined as the ratio of the refractive index sensitivity to the resonance width Δλ:

$$FOM = \frac{S(nm/RIU)}{\Delta\lambda(nm)} \qquad (2\text{-}11)$$

Resolution is typically defined as the minimum detection limit. It can be improved by the size and the geometry of nanostructures.

One of the earliest LSPR sensor nanostructures was the simple-shaped nanoparticles made of gold or silver with the aspect ratio of 2. However, the electromagnetic field strength is weak and field distribution is not confined to certain point so that it does not seem to be effective for small bio-molecules detection. One of the notable ways to build a LSPR sensor with higher sensitivity is to change the shape of nanospheres in order to ignite multiple resonances. As we know, the size and the shape of metallic nanoparticles contribute to spectral properties due to the changes in surface polarization. Diverse shapes with the increase of aspect ratio such as triangles, cubes, prisms, bars, rods have been synthesized to tailor LSPR from visible to infrared region and are able to exhibit several separate resonance peaks. [5] The size of the nanoparticles influences the relative magnitude of the absorption and scattering of the cross section. For particles smaller than 20nm, the predominant process is absorption. As the size increases, the scattering becomes major effect. In general, the sensitivity is more dependent on spherical geometry than size. [16] For instance, changing the size from 10 to 100 nm for nanosphere results in red shift of 47 nm, while change of aspect ratio from 2.5 to 3.5 results in shift of longitudinal mode by 92nm. [17] The key interest in selection of various shapes is to create “hot spot” region which refers to the enhancement of localized and confined electromagnetic field. Hot spots generated at nano-scale sharp tips can provide localized molecular sensing with the greatest sensitivity and resolution. Van Duyne and his coworkers [18] fixed a single silver nanoparticle to a glass coverslip in solvents with increasing refractive index to study the behavior of detecting dielectric environment change. It was estimated that a fully assembled octanethiol monolayer covering the particle with a surface area of 14,000 nm^2 has 60,000 molecules on its surface. At 1 mM saturation, octanethiol produced a shift of 8 nm, for an average shift of 10^{-4} nm per molecule. Nanorods have been examined experimentally to offer greater sensitivity to refractive index changer than that observed from nanospheres. The longitudinal mode for a nanorod with aspect ratio of 3 was shown to have six times higher sensitivity. [19] The biosensing

ability in avidin-biotin interaction provided a limit of detection of 94 pM in buffer solution and 19 nM for serum samples. The dynamic range for this assay spanned almost six orders of magnitude from 94 pM to 0.19 uM. [20] A single silver triangular nanoprism was reported to yield a spectral shift of 4.4 nm per additional CH_2 unit on linear alkylthiol which is considerably higher than a single silver nanosphere. [21]

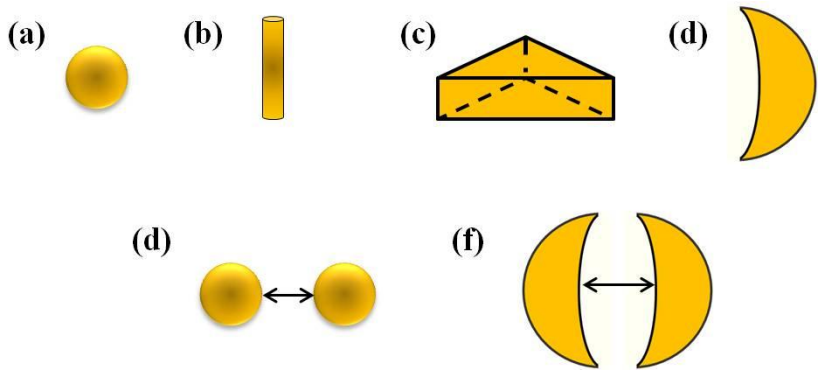

Figure 2-6 (a) Nanosphere (b) Nanorod (c) Nanoprisum (d) Nanocrescent (d) Intercoupling of nanospheres with a distance of several hundred nanometers (d) Double nanocrescents facing each

In attempt to achieve additional field enhancement, intercoupling between two particles has been proposed. In this method, two nanoparticles are brought into vicinity of each other creating a nanogap smaller than the wavelength of light. In this manner, the near-field dipolar interactions prevail as a dipole field in one nanoparticle induces oscillations in an adjacent naoparticle producing “hot spot” region in the proximity between them as well. Such LSPR enhancement effect becomes stronger as the particles get closer. Double nanocrescents structure facing each other is a good case to study the combined effect of both multiple resonances and inter-coupling of nanoparticles. [22] As we know, single nanocrescent is able to generate structure polarizability at the sharp tips when illuminated with vertically polarized light due to the concept mentioned before, that more needle-like structure can strongly enhance the field. When two nanocrescents are placed with the tips very close to each other, the enhanced field intensity calculated is approximately two times larger than that of single nanocrescent in vertically polarization case.

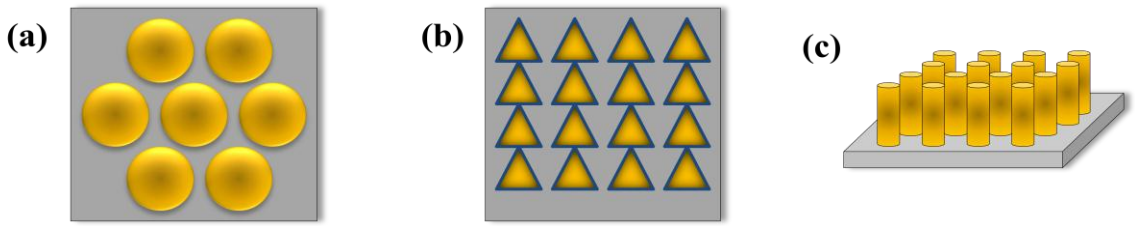

Figure 2-7 (a) Nanosphere arrays (b) Triangular nanoprism arrays (c) Nanorod arrays

Extended from this phenomenon, nanoparticle array structure as well as its inverse structure has been proposed to act as a bulk refractive index sensor. The earliest efforts made use of silver or gold periodic nanosphere arrays, using biotin-avidin interaction for immobilization of biomolecules. Optimization of the size of nanospheres achieved a limit of dectection (LOD) for the avidin of 0.83nM [23] and smaller molecules such as the steroidal hormone stanozol of 2.4 nM. [24] Ag triangular arrays also provide a good platform to investigate binding event. ADDL ligand antigen was immobilized on the surface coated with a monolayer of bonding. Then, the binding event of antibody was studied, and the associated saturation of LSPR response yielded an 18.5 nm shift at a concentration of 100 nM of antibody. [25] In a separate study, 43 nm citrate capped colloidal gold nanoparticles were immobilized on a quartz substrate and further integrated into microfluidic device. A sensitivity of 62nm/RIU is measured using glycerol solution. [26] Plasmonic nanorod arrays produced by Kabashin's group provided an enhanced sensitivity (30000nm/RIU) to refractive index variation of the medium between the rods using a standard avidin-biotin affinity model.[27] This extremely high sensitivity benefited from the overlap between the probing field and the strong plasmon-mediated energy confinement within the nanorod layer. More interestingly, significant improvement of an LSPR bioassay with 400% amplification of shift upon antibody binding was demonstrated on a biotin functionalized silver nanoprism array using 20 nm gold nanoparticle labeled antibodies. The induced wavelength shift was 42.7 nm while unlabeled antibody resulted in a decent red shift of 11 nm.[28]

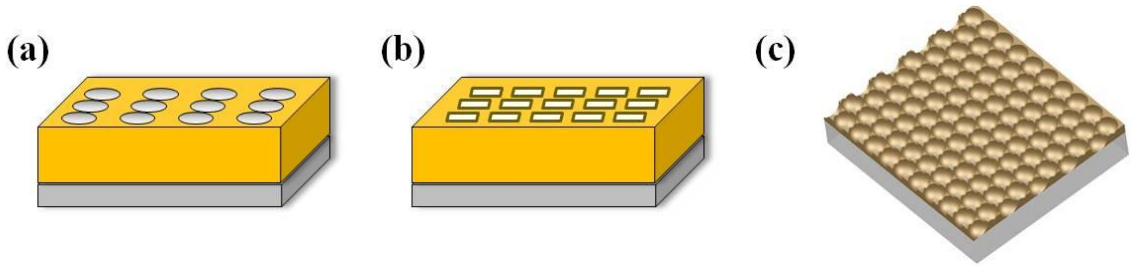

Figure 2-8 (a) Round nanohole arrays (b) Square nanoprism arrays (c) Film-over-nanosphere structure

Emerging from lithographical technologies, the inverse structures of nanoparticle arrays, called films-over-nanosphere (FON) structures, have drawn a lot of attentions from scientists and researchers. Such nanopatterned film serves as “roughened” surface with larger proportion of void space enabling increased detection volume of biomolecules. Meantime, plasmons are well confined in cavities and energy overlapping can be reached due to the periodicity of the voids. Such collective enhancement of electromagnetic field make “hot spot” region possible within the cavities and contribute remarkably to the refractive index sensing performance. Among all of these FON structures, nanohole arrays have been deeply studied. It has been observed that isolated holes in a conductive film can modify the transmission of the light due to plasmonic effect. [29] A much greater optical effect is seen for periodic arrays of isolated holes. This is given rise from an extended LSPR if the holes are of a size smaller than the wavelength of the incident light and each hole as a point source is within the decay length of surface plasmons such that the plasmons can overlap and interact. [30] The structure parameters such as the size, shape, density and periodicity have been thoroughly looked into to understand the relation between structure and LSPR. Generally, a similar spectral outcome is observed whether the geometry of a hole is square or round. Larger holes can transmit more light up to a size of about 200 nm. A constant pitch of about 600 nm for holes of 200 nm will result in transmission of optical radiation at about 700 nm. [31] The sensitivity of nanohole arrays is typically 200 to 300 nm per refractive index unit. Ferreira and coworkers fabricated 30 × 30 nanohole arrays and monitored the biosensing behavior based on biotin-avidin model. It yielded a 10 nm LSPR shift assuming full

coverage of each hole with about 2000 molecules probed. [32] Moreover, Henzie and coworkers reported a FOM of more than 23 and a good sensitivity of about 300 nm/RIU for ordered gold arrays of nanoholes by soft interference lithography. [33] Hicks and coworkers developed a plasmonic structure termed “film over nanowell” by reactive ion etching through nanosphere lithography followed by the removal of the mask. The structure exhibited plasmon peaks with a full width at half maximum (FWHM) as narrow as 35 nm, and a sensitivity of 538 nm/RIU with an overall FOM of 14.5, surpassing that of typical nanoprism arrays of about 3. [34]

2.1.3 Optical Fiber based Plasmonic Biosensor

LSPR instruments are usually home built and designed for a specific experiment or application. They typically consist of three components: a light source (white light or laser), a sample stage and a detector. For transparent samples, light is transmitted directly through the sample and the detector is placed on the other side. For non-transparent samples, an optical geometry suitable to study reflection is used. For instance, nanohole arrays have been well studied in transmission mode, and extraordinary transmission is observed. FON substrates are usually configured in a reflection mode to study their plasmonic properties. Unfortunately, as for plasmonic sensing application, analytical solution has to been sampled out for measurement. It is inconvenient and lack of timeliness. With the help of optical fiber, miniaturization of an LSPR sensor system has become possible. One of the important advantages of integrating the LSPR nanostructures into an optical fiber is its capability for remote sensing and in situ/in vivo sensing. Other advantage is its very small sample volume.

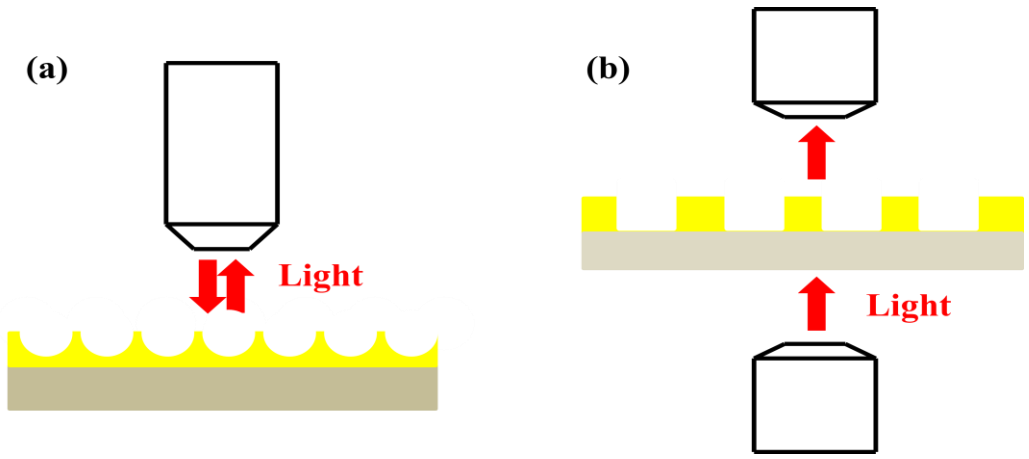

Figure 2-9 (a) Reflection mode for FON structure (b) Transmission mode for nanohole arrays

Optical fiber sensors have been a continuous research topic for a long time. Optical fiber LSPR sensors are basically similar to the Kretschmann's prism structure mentioned before, where the prism is replaced with a fiber core after the cladding has been etched off. Then, the fiber core is symmetrically coated with metal for the excitation of SPP on its surface. Recalling the phase matching condition of prism coupling, we obtain:

$$k\sqrt{\varepsilon_{fiber}}\sin\theta = \frac{\omega}{c}\sqrt{\frac{\varepsilon\varepsilon_m}{\varepsilon+\varepsilon_m}} \qquad (2\text{-}12)$$

where ε_{fiber} is the dielectric constant of the fiber core and ε, ε_m are that of the metal coating and its sample medium respectively. SPP can be excited at the interface in this easy and flexible manner, and it is very sensitive to any change of refractive index of sample medium due to the surface condition change such as the adsorption of molecules. The change of ε_m will lead to a change of incident angle or wavelength to regain the phase matching condition.

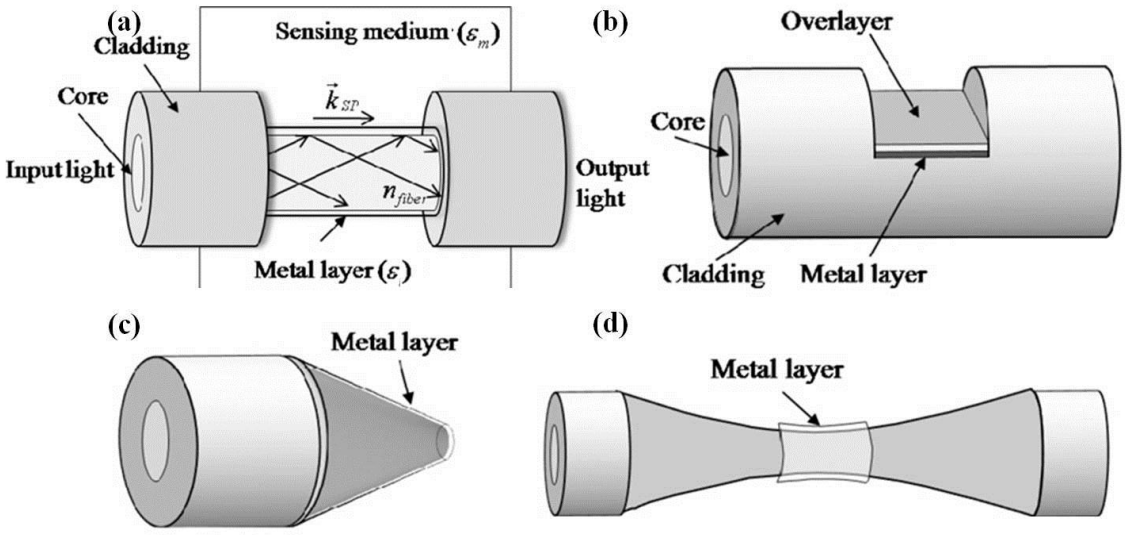

Figure 2-10 (a) Cladding-off fiber probe (b) D-shape fiber probe (c) Angled fiber probe (d) Tapered fiber probe

So far, there have been various fundamental SPR fiber sensor configurations. These include symmetrical structures, such as simple metal coated optical fiber, [35] tapered fiber structures without any symmetry, [36] such as side polished fibers (or D-shape fiber) and one-side metal coated fibers, [37] and structures with modified fiber tips with flat or angled structures. [38] Besides, many SPR fiber sensor systems have also been developed with structures that have been further modified, via the use of several types of gratings, hetero core fibers, nanoholes and so on. In order to develop these SPR fiber sensors, the fiber cladding is completely or partially removed. After exposing the fiber core region, a metal layer needs to be placed above it. This can be realized by either thermal deposition of metal bulk or chemical immobilization of nanoparticle colloids. The former is usually used for developing traditional SPR sensor while, the latter is normally for novel nanostructure LSPR sensor.

Here, we are going to examine a couple of parameters that affect the characteristics of SPR sensor. First of all, a fiber, either single mode fiber (SMF) or multiple mode fiber (MMF) should be suitable for particular purpose. An SPR sensor with MMF exhibits fluctuation of the output signal due to the mechanical disturbance. However, it provides a good signal-to-noise ratio and a wide range of refractive index for measurement. On the other hand, a sensor with SMF

generally has a narrower resonance dip than that with MMF and hence has good accuracy. Second, the fiber sensor with a modified fiber tip is usually used as a reflection-based SPR fiber probe, while other types of SPR fiber sensors are in a transmission manner. Third, as mentioned above, the metallic layer used in SPR sensor is typically gold or silver. Gold demonstrates a high resonance shift in response to the refractive index change and a high chemical stability. Silver displays a narrower extinction peak, therefore high resolution, but is unstable in the presence of air and water. As a result, a thin and dense protection overlayer, who is also able to tune the resonance wavelength, is placed to increase the reliability. At last, the thickness of the metal layer is extremely critical for a SPR sensor. A thin film, less than 100nm, should be used, because the evanescent field decays exponentially in the metal layer. Generally speaking, the optimization of the metal layer thickness is required for a SPR sensor with narrower and deeper curve, in another word, higher FOM.

Typically demonstrated SPR fiber sensors show the dielectric sensitivity in the range of several thousand nanometers per refractive index unit with gold coating. Recently, many novel SPR sensors adopting photonic crystal concepts have been proposed to have better sensitivity. The photonic crystal fiber (PCF) has a dielectric structure, typically nanohole arrays or similar, whose periodicity is on the order of visible light wavelength at the end or side of optical fibers, giving rise to the photonic bandgap. The incident light whose wavelength lies within the photonic bandgap cannot propagate through and the transmission spectrum exhibits an extinction peak. By locally breaking the period at the core, a photonic defect mode is introduced resulting in a sharper transmission peak, which is highly sensitive to the dielectric environment change. Once liquid or gas molecules are adsorbed to the defect, a transduction signal shift can be sensed. Due to its good structural flexibility to adjust the defect mode across the photonic bandgap, PCF sensors have received huge attention. [39]

2.2 Formation of Colloidal Crystals

Dispersions of colloids have been prepared and processed since the very beginning of the human civilization such as concentrated clay dispersion for pottery around 7000 BC. Recently,

with the blossom of nanotechnology, submicron or nanometer colloids, mainly polymer and silica, with sizes ranging from tens of nanometer to several microns have become commercially available in a large amount with an exceedingly uniform size distribution. Colloidal particles, under certain condition, are able to self-organize on the surfaces to form periodic 2D or 3D colloidal crystal. Inspired by the special optical property of natural opal, this “artificial” opal finds its application in photonics and plasmonic sensors. Here, the characteristics of colloid and the mechanisms of self-assembly of patterns will be discussed.

2.2.1 Colloidal Solution

A colloid is a substance (internal phase) microscopically dispersed evenly throughout another substance (continuous phase). A colloid solution is a liquid colloidal system. For example, milk is an emulsified colloid of liquid butterfat globules dispersed within a water-based solution. Unlike the solution, which is composed of only one phase with the solute particle size less than 1 nm, the particles uniformly dispersed in colloid solution are from 1 nm to 1000 nm.

Electrostatic stabilization and steric stabilization are the two main mechanisms for stabilization against coagulation. Generally speaking, different phases have different charge affinities, so that an electrical double layer forms at the interface between solute and solvent. This effect becomes significantly amplified in colloids because small particles lead to enormous surface area. Since the mass of the dispersed phase is so low, its buoyancy or kinetic energy becomes negligible comparing to the electrostatic repulsion between charged layers of the dispersed phase. Therefore, particles do not stick together and are able to stay in the solution. This is called electrostatic stabilization. The other mechanism, steric stabilization, is achieved by polymer molecules attached to the particle surface preventing the coagulation of the particles in the range of attractive forces. In this study, the colloidal particles used are polystyrene particles. The theory and principle of electrostatic stabilization will be explained in details in the following sessions.

2.2.2 Electrostatic Stabilization and DLVO Theory

Nowadays, a variety of colloidal particles with positive or negative charges directly created on the surfaces during synthesis process to increase the dispersive property are commercially available using electrostatic stabilization. In 1940s, Deryagin, Landau, Vewey and Overbeek developed a theory (DLVO theory) to systematically study the stability of colloidal systems. It has following assumptions:

- The colloidal solution is a diluted dispersion.
- There are only two forces acting on the dispersed particles: Van der Waals force and electrostatic force.
- The electric charge and other properties are uniformly distributed over the solid surface.
- The distribution of the charge is determined by the electrostatic force, Brownian motion and entropic dispersion.

According to the assumption, the theory combines the effects of van der Waals attraction and the electrostatic repulsion due to the double layer of counterions. For ordinary condition, the mathematical derivation of the theory can be simplified by adding these two parts together.

In physical chemistry, the van der Waals force is the sum of the attractive force between molecules including dipole-dipole force (Keesom force), dipole-induced dipole force (Debye force) and dispersion force (London force), which is the most important of three. The pair potential between two atoms or small molecules has the form of $w(r) = -C/r^6$, where C is the interaction energy constant, r is the radius of the atom/ molecule. With another assumption of additivity, the net interaction energy for a molecule at a distance D away from the surface will be

$$W(D) = -\pi^2 C\rho_1\rho_2 R/6D \qquad (2\text{-}13)$$

where W (D) is the interaction energy between the sphere and the surface, ρ_1 is the number density of the surface and ρ_2 is the number density of the sphere, R is the radius of the sphere. With Hamaker constant $A = \pi^2 C\rho_1\rho_2$, the equation will be simplified to

$$W(D) = -AR/6D \qquad (2\text{-}14)$$

Similarly, according to Derjaguin approximation, the van der Waals interaction between spheres and surfaces can be calculated and summarized as below

Two spheres $W = -\frac{A}{6D}\frac{R_1 R_2}{(R_1 + R_2)}$ (2-15)

Sphere-surface $W = -AR/6D$ (2-16)

Two surfaces $W = -A/12\pi D^2$ per unit area (2-17)

A double layer, also called an electrical double layer EDL, is the layer surrounding the particle of the dispersed phase and including the ions adsorbed on the surface of the particle and a film of the countercharged dispersion medium. When a surface is placed in the liquid, it may be charged by dissociation of surface groups or by adsorption of charged ions in the solution. This results a wall surface potential which will attract counterions and repel co-ions. In steady state, the surface charge is balanced by oppositely charged counterions. The EDL, which, therefore, is electrically neutral, refers to these two parallel layers of charge around the particle. It consists of three parts. The first layer, the surface charge (commonly negative), comprises the ions adsorbed directly onto the particle surface. The second layer, which is called Stern layer or Helmholtz layer, is composed of ions strongly bound to the surface charge via the Coulomb force, electrically screening the first layer. The layer adjacent to second layer contains loosely associated ions which are comparatively mobile. They move in the fluid under the influence of electric attraction and thermal motion rather than being firmly anchored. Thus, it is called the diffuse layer.

There have been several theoretical treatments of electrical double layer. They will be interpreted for the derivation of double layer potential. The earliest model of EDL is attributed to Helmholtz who treated the second layer as a simple capacitor. Thus, the electrostatic potential can be expressed as Poisson-Boltzmann equation

$$\nabla^2 \psi = -\frac{e}{\varepsilon_r \varepsilon_0} \sum_i z_i \rho_{0i} \exp\left(-z_i e \psi / kT\right) \qquad (2\text{-}18)$$

where ε_r is the dielectric constant of medium; ε_0 is the permittivity of free space; ψ is the electrostatic potential; z_i is the valence of ion species; ρ_{0i} is the concentration of ion species in the bulk. The Helmholtz theory does not adequately explain all the features, since it hypothesizes rigid layers of opposite charges. This does not occur in nature.

Later, Louis Georges Gouy and David Chapman made significant improvements by introducing a diffuse model to EDL. They suggested that counterions are not rigidly held, but tend to diffuse into the liquid phase causing the exponentially decrease of electric potential. The general relation between the surface charge density and ionic concentrations at the surface and in the bulk, as Grahame equations is obtained.

$$\sigma^2 = 2\varepsilon_r \varepsilon_0 kT \sum_i \{\rho_{\infty i}[\exp(-z_i e\psi_s / kT) - 1]\} \qquad (2\text{-}19)$$

There are only a small number of cases for which simple solution to the Poisson-Boltzmann equation can be found. However, for surface potential below 26 mV, Grahame equation is simplified via Debye-Huckel approximation to

$$\sigma = \varepsilon_r \varepsilon_0 \kappa \psi_s \qquad (2\text{-}20)$$

where $\kappa = (\sum_i \rho_{\infty i} e^2 z_i^2 / \varepsilon_r \varepsilon_0 kT)^{1/2}$, is called Debye screening length. It is a very important characteristic of the repulsive electrostatic interaction between particles and refers to the thickness of the diffuse electric double layer. With proper mathematical treatments, the double layer interaction energy can be summarized as below

Two planes $W = (64 k_B T \rho_\infty \gamma^2 / \kappa) e^{-\kappa D}$ per unit area (2-21)

Two spheres $W = (64\pi k_B T R \rho_\infty \gamma^2 / \kappa^2) e^{-\kappa D}$ (2-22)

where γ is the reduced surface potential and has the form of $\gamma = \tanh(\frac{ze\varphi_0}{4kT})$.

Combining the van der Waals interaction energy and the double layer interaction energy, the interaction between two particles or two surfaces in a liquid can be expressed as

$$W(D) = W(D)_A + W(D)_R \qquad (2\text{-}23)$$

where $W(D)_A$ comes from the van der Waals attraction and $W(D)_R$ comes from electric double layer repulsion.[40]

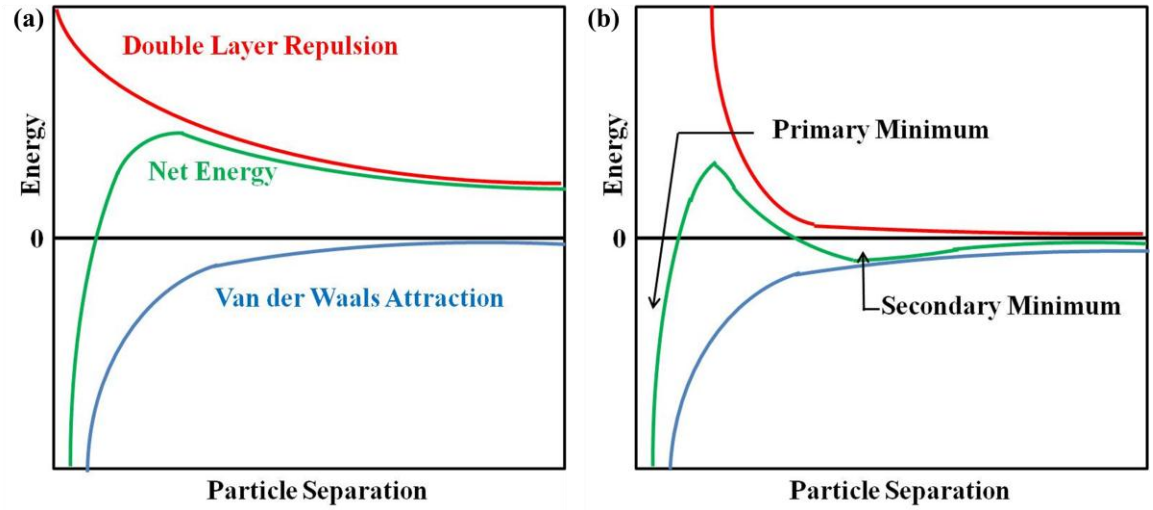

Figure 2-11 (a) Sketch of energy vs distance profiles in DLVO theory (b) Primary minimum and secondary minimum in energy profile

As shown in Fig. 2-11 (a), the stability of the colloid system is determined by the sum of these two forces between particles as they approach each other due to the Brownian motion they are undergoing. The energy barrier resulting from the repulsive force prevents particles from adhering together. But if the particles collide with sufficient energy to overcome the barrier, they will stick irreversibly together. In a more concentrated salt solution, there is a possibility of a "second minimum" where a much weaker and potentially reversible adhesion between particles exists together in Fig. 2-11 (b).

Since 1940s, the DLVO theory has been used to explain phenomena found in colloidal science, adsorption and many other fields. It has become even more popular with the merging of nanoscale science, because it can be used to explain both general nanoparticles and microorganisms. However, DLVO theory is not effective in describing ordering process such as the evolution of colloidal crystals in dilute dispersions with low concentration.

2.2.3 Colloidal Crystal and Self-assembly

A colloidal crystal is an ordered array of colloid particles. A prominent example of colloidal crystals in nature is the gemstone opal, which contains a natural periodic microstructure of silica microspheres responsible for its iridescent color. Typical colloidal crystals are ordered arrays of highly monodisperse silica or polymer mircospheres, which yield periodic, spatial variations in dielectric properties on the submicron length scale. Bragg diffraction of light within these colloidal crystals gives rise to a stop-band, in which the propagation of light within a narrow range of wavelengths in specific directions is prohibited. Crystal quality and crystal lattice are among the most important characteristics determining the performance of colloid crystals in optical application. Colloidal crystals normally contain numerous defects such as vacancies, dislocations, stacking faults and grain boundaries. Thus, their degree of structural perfection and optical quality must meet an exceptionally high standard in order to achieve better performance. Of special interest is the crystal lattice or packing order of colloidal crystals. Although most colloidal crystals prepared are stacked as entropy favorable face-centered cubic (FCC), hexagonal closed packed (HCP), or combine as random hexagonal closed packed (RHCP) structure, many other complex crystal structures could be fabricated by controlled or templated self-assembly.

Self-assembly strategy is known as the most feasible route to fabricate two-dimensional (2D) or three-dimensional (3D) colloidal crystals. It is the process by which nanoparticles spontaneously organize into ordered structures driven by specific interactions. [41] In recent years, various self-assembly techniques of polystyrene particles have been developed to fabricate colloidal crystals with high quality and complicated structures including gravity sedimentation, vertical deposition, physical confinement and external field induction. Along with their mechanisms, they will be reviewed here.

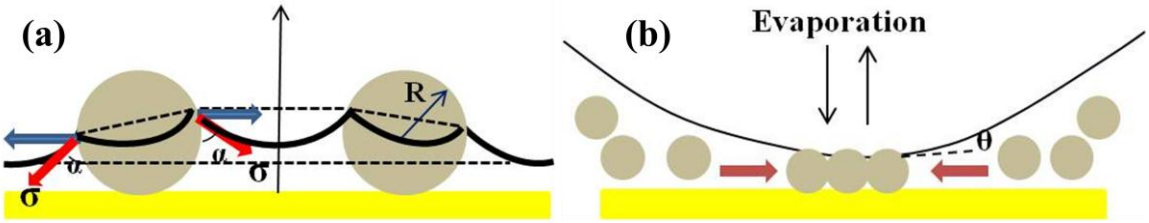

Figure 2-12 (a) Sketch of inter-particle attraction for nucleation (b) Sketch of crystal growth by convective flow of particles

Self-assembly of colloidal particles is a complicated interaction process involving gravity, electrostatic repulsion, and Brownian motion. Back in 1990s, Denkov et al. first uncovered that capillary force and convective interaction are two major driving forces in the self-assembly process. [42] Fig. 2-12 (a) and (b) shows schematically the formation process of the colloidal crystal. At first, a nucleus was formed when the thickness of the liquid layer approached the diameter of the particles due to the evaporation of the water. Then more particles were transported towards the nucleus by convective fluid, and eventually formed a 2D hexagonally packed array. There are several crucial factors that will affect the quality of the periodic arrays. Air pressure, temperature and the choice of the solvent all determine the evaporation speed of the solvent and control the rate of self-assembly. High humidity is often preferred to enhance capillary force between particles to produce colloids with fewer defects, but it lengthens total time of self-assembly. Based on these assembly forces, several assembly approaches have been developed to control the assembling of the latex particles.

The earliest assembly method is gravity sedimentation. [43] Silica particles were used to settle in a gravitational field due to their density. Even though this method has been improved by optimized process such as high vacuum filtration and centrifugation, it still suffers long deposition time, numerous defects and lack of control on the thickness.

Currently, the most popular self-assembling strategy is to organize the colloidal particles by vertical deposition. [44] In this method, a vertical glass substrate which is put into the latex suspension is pulled upward slowly. The particles would be transferred by capillary attraction and convective particle flux towards the glass during evaporation. Thus, the balance between capillary

force and convective flux is the key for the colloid crystallization. Much effort has been made to optimize the process of vertical deposition for higher quality colloidal crystal. [45-48] Vertical deposition technique has been proved to be able to produce highly ordered crack-free colloidal crystal with controllable thickness.

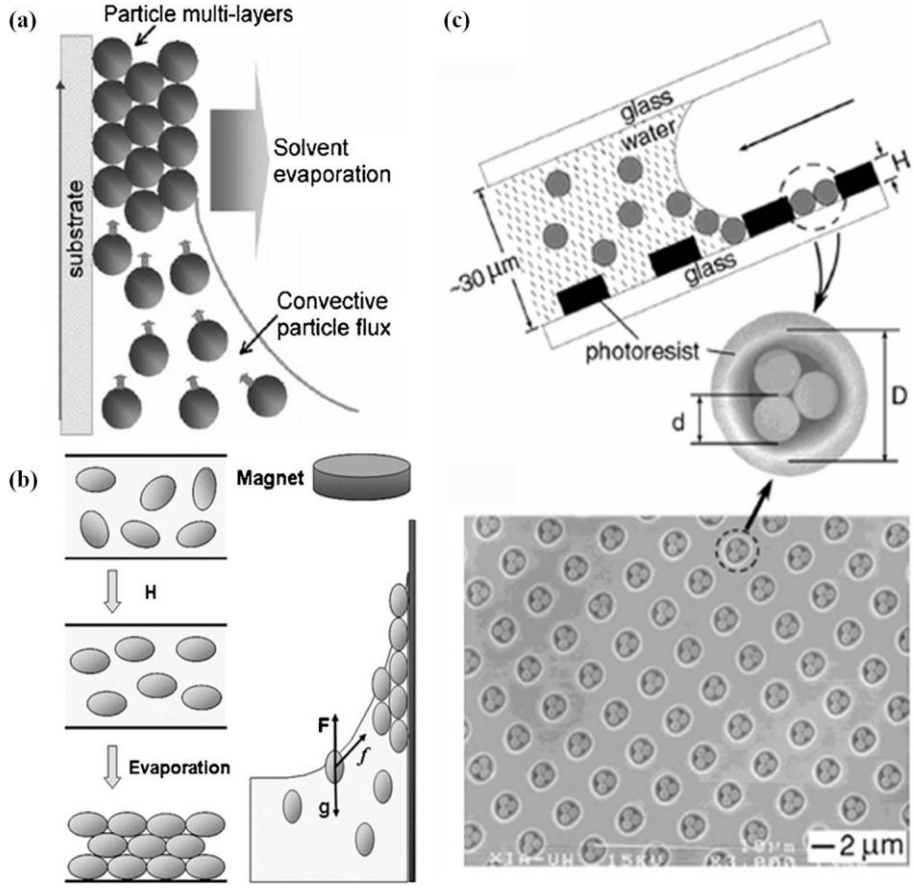

Figure 2-13 (a) Vertical deposition of multilayer colloids (b) Self-assembly in magnetic field (c) Colloidal crystal fabricated in physical confinement

Colloidal crystals can also be fabricated under certain physical confinement. Usually, special confinements are designed such as cylindrical hole, square, triangular and noncircular patterns to fabricate a series of complex aggregates of monodisperse colloids with well-defined sizes, shapes and structures. The advantages of the physical confinement method are the abundant choice of substrate with different shapes and the shape dependence of the resulting colloidal crystals with the substrates.

Exterior fields such as electric or magnetic fields are significant tools to assemble colloidal particles.[49] An alternating electric field can induce crystallization of highly charged monodisperse particles between two electrodes based on field intensity gradient. The assembly process can be controlled by the field strength, frequency, and the viscosity of the liquid media. Magnetic field has also been widely used for fabrication.[50] Emulsion droplets containing magnetic (superparamagnetic) nanoparticles self-assemble upon application of external magnetic field. Furthermore, these magnetic nanoparticles covered with a layer of silica dispersed in various polar organic solvents, such as methanol and ethanol are also allowed to assemble into ordered structure with magnetic field. Other assembly techniques consist of interfacial self-assembly and printing. The former refers to an equilibrium assembly process related to surface tension, density and hydrophobicity/hydrophilicity. The latter utilizes the attractive force to pick up a small volume of colloidal suspension with a pin and transfers it to a defined position on prestructured substrates and let it order into a periodic array under controlled humidity condition.

With continuous attention paid to colloidal crystals, scientists and researchers find that it is promising for a wealth of practical applications in optical devices. The colloidal crystal with periodic structure is able to affect the propagation of the light. Photons with specific wavelength are prohibited to travel through forming the photonic band gaps. Hence, the opal serving as photonic bandgap material gives rise to distinct optical functions such as inhibition of spontaneous emission, high reflecting omni-directional mirrors and low-loss waveguiding. Meantime, metallic inverse opal has been explored for its huge potential as plasmonic sensor. The “honeycomb” with the embeded spherical pattern can couple to light and become colored due to surface plasmon absorption. The electromagnetic fields are strongly confined into the nanocavities resulting in localized plasmon modes. It is very sensitive to the surface feature and thus can be directly exploited for plasmonic sensor and surface enhanced Raman spectroscopy.

2.3 Computational Simulation in Finite-Difference Time-Domain (FDTD) Method

In real world, electromagnetic problems such as scattering, radiation, wave guiding etc., are not analytically calculable because irregular geometries found in actual device. Computational

numerical techniques can overcome the inability to derive solutions of Maxwell's equations under various constitutive relations of media, and boundary conditions. Computational electromagnetics (CEM) is the process of modeling the interaction of electromagnetic fields with physical objects and the environment. It is very important for designing and calculating the performance of antenna, radar, satellite and other communication systems, high speed silicon electronics, medical imaging, cell-phone antenna design, and other applications. A specific part of CEM deals with the electromagnetic radiation and propagation in small and complex structures.

CEM typically solves the problem of computing the E (electric), and H (magnetic) field across the defined problem domain. CEM model simplifies real world structures to idealized cylinders, spheres, and other regular geometrical objects. Furthermore, it extensively makes use of symmetry, and solve for reduced dimensionality from 3D to 2D or even 1D. The basic approach is to discretize the space in terms of grids (both orthogonal and non-orthogonal) and solve Maxwell's equations at each point in the grid. Discretization consumes large computer memory and solving the equations takes long time. Nowadays, solving CEM problems require supercomputers, high performance clusters, vector processors and parallel computer.

In terms of different forms of Maxwell's equation, there have been two major methods solving the problem, which are integral equation solver and differential equation solver. The method of moments (MoM) or boundary element method (BEM) is a numerical computational method in the former category. It requires calculating only boundary values by meshing over the modeled surface, rather than values throughout the whole space. It is a lot more efficient in terms of computational resources for problems with a small surface/volume ratio. However, when it comes to large analyzing volume, the efficiency and reliability drops dramatically. By contrast, volume-discretization methods such as finite element method (FEM) and FDTD take good care of the problem associated with curved geometrical objects.[51]

FDTD is a widespread method for finding approximate solutions to Maxwell's equation in differential form. It belongs in differential time-domain numerical modeling methods. The time-dependent Maxwell's equations in partial differential form are discretized using central-difference

approximations to the space and time partial derivatives. Then the equations are implemented in a software and solved in a cyclic manner: the electric field vector components in a volume of space are solved at a given instant in time, the magnetic field vector components in the same spatial volume are solved at the next instant in time. Such process is repeated over and over again until the desired transient or steady-state EM field behavior is fully evolved. The FDTD method has a couple of important advantages. It is able to cover a wide range of frequency in a single simulation using Fourier transform. It treats the simulated structures with a wide variety of EM material properties. Both time domain and frequency domain information are offered for unique insight into all types of problems and applications in electromagnetics and photonics.

Here, we demonstrate the procedure of performing a simulation using commercial FDTD software from Lumerical Solutions, Inc.

Step 1: Create Physical Structures

The structures with various shapes and arrangements of object are available, the properties of them can be set via the edit tool. Each object can be defined its own material properties by selecting from the extensive materials database or by user-defining. Dielectric, metallic and dispersive materials are supported.

Step 2: Set Simulation Region and Time

The simulation region is the region over which the calculation is performed. The location and size of the region must be set, the mesh accuracy chosen and the appropriate boundary conditions must be specified. Since frequency domain information is calculated by a Fourier transform of the results obtained in the time domain, it is necessary that the simulation time is set long enough that the results have converged.

Step 3: Define Sources

Different types of source are available for use depending on the application, e.g. point dipole useful for exciting modes in cavities and resonators, Gaussian beam and plane wave for textured surface, total field scattered field for particle scattering. Once created, source properties like location, size, and propagation direction can be edited as required.

Step 4: Define Monitors

Monitors are used to record the electromagnetic fields required for subsequent plotting and data analysis. Different types of monitors are available depending on the application and the required results. In addition to the basic monitors, the complex monitors (called analysis groups) comprised of basic monitors and a script to process monitor data also can be created for use.

Step 5: Run Simulation

Once the simulation objects have been created, the FDTD simulation file can be saved and run. The memory requirements for a particular simulation can be checked from the Check Memory Requirements on the simulation menu. The number of mesh points, where the electric and magnetic field as well as the material properties are stored, is highly related to the memory requirements. The monitors used also increase memory requirements substantially.

Step 6: Plot Results and Analyze Data

The data produced by each selected monitor, after running the simulation, were stored in the file and can be used for the analysis. For example, the electric field intensity can be obtained from the frequency domain field profile monitor. The results can be plotted or exported to a text file for further use. The scripting language allows for much more advanced analysis than the graphical analysis window.

CHAPTER 3

EXPERIMENTAL

In this chapter, the formation of polystyrene nanosphere crystal templates is described. Then, electroplating of metals into the templates is introduced. After that, the design and fabrication of optical fiber based plasmonic sensor in a reflection manner is explained. Homemade optical instrument is presented and certain experimental measurements are carried out. Finally, FDTD Solutions is used to simulate optical behavior of the nanostructure.

3.1 Formation of Colloidal Crystal Template

The fabrication process of a colloidal template with monodispersed nanospheres involves two steps: (1) Preparation of gold substrate (2) Self-assembly of Polystyrene nanospheres.

3.1.1 Preparation of Gold Substrate

As mentioned before, self assembly process of polymer particles can be performed on a number of substrates such as SiO_2, Au, Ag or even Hg. Here, the gold coating serves three purposes. First, gold is widely used in bioengineering field for its chemical stability and good compatibility with human tissue. Second, the self assembled template on gold substrate contains fewer defects such as stacking faults, cracks and dislocations than other substrates, also it is quite robust regarding its adhesion to the surface. Third, the thin film is able to provide a decent conductive working electrode for electrochemical plating later.

The gold coated substrate is prepared by thermal evaporation of 5 nm of chromium, followed by 7 nm of gold onto 400 μm thick prime grade 3" silicon wafer (NOVA Electronic Materials, LLC) or 100 μm thick micro cover slip (VWR International) in a high vacuum of 5 μTor with a deposition rate of 2 Å/s. The Si wafers are thoroughly cleaned before evaporation by rinsing with acetone followed by isopropanol alcohol (IPA) and deionized water (DI water), and then dried under a gentle stream of N_2. The gold coated Si wafers are cleaved into 1.5 cm × 1.5 cm small square pieces to provide individual surfaces for self-assembly of PS nanospheres.

3.1.2 Self Assembly of PS Nanospheres

As mentioned in the previous chapter, there have been various well developed self-assembly techniques. Here, the formation of multilayer colloidal crystal templates is realized by humidity-controlled horizontal deposition of monodispersed PS nanospheres in a physical confinement. The self-ordering process is carried out in a setup which is made up of Viton rubber o-ring (1.2 cm diameter), a Teflon washer (0.9 cm inside diameter, 2 cm outside diameter) and prepared 1.5 cm × 1.5 cm gold coated substrate stacked tightly from top to bottom as shown in Fig. 3-1 (a).

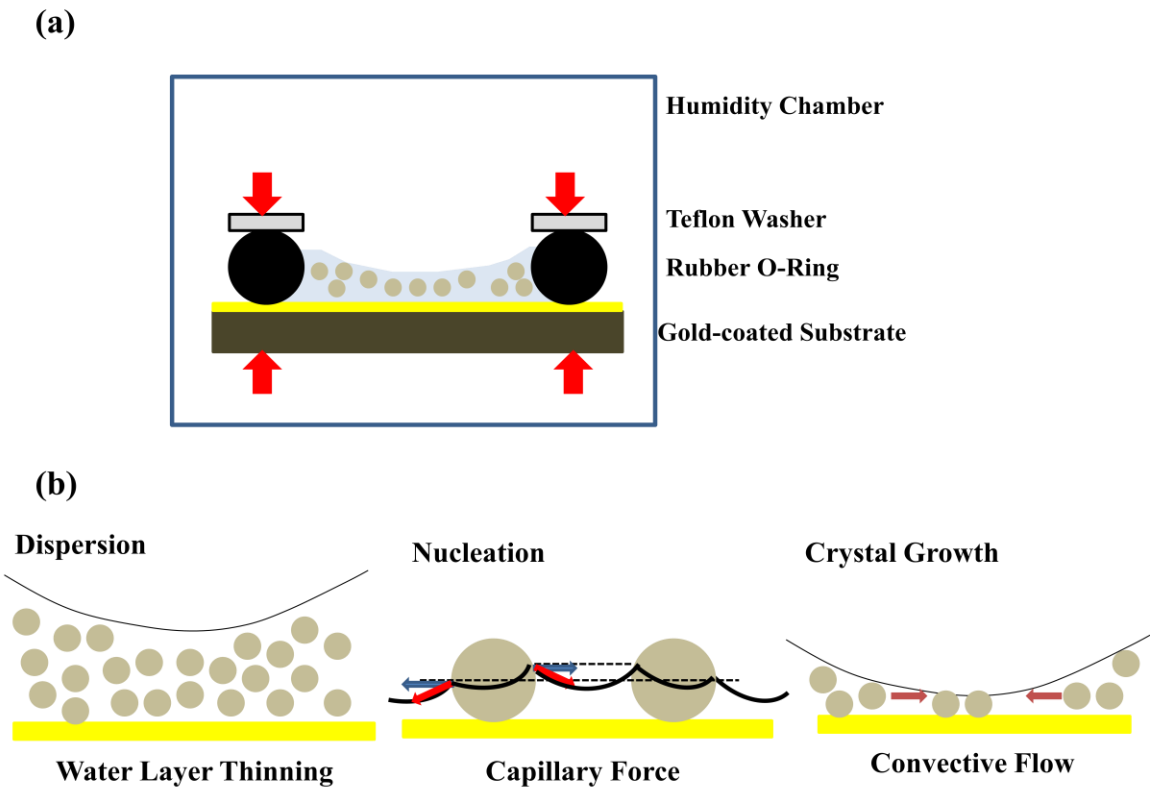

Figure 3-1 (a) Set up of physical confinement method for self assembly (b) Three stages of self assembly

About 200 µL of colloidal solution is injected to each cell. It is made of 2.6 wt. % monodispersed PS microsphere suspension (Polybead®, Polyscience, Inc) diluted with DI water with a volume ratio of 1:5. The available sizes of PS particles for template formation range from 100 nm to 1000 nm with standard deviation within 15 nm. Then, the cell is held horizontally in an

incubator with controllable humidity for appropriate rate of evaporation from the cell. Empirically speaking, the inside environment is set to have a relative humidity of 75% at the first place in order to make the incubator humid enough then well maintained at around 55% for about 48 hours. After drying the template appears opalescent with colors from green to red, depending on the particle size and the angle of observation, clearly visible when illuminated from above with white light. As an artificial opal, it emits six light rays with same color radially. Such structural color arises from Bragg's diffraction of the light in the hexagonally close-packed arrangement of micospheres. The templates are robust and adhere well to the gold substrates. There is no evidence for re-suspension of the particles when placed in contact with electroplating solutions. The self-organize process results in a close-packed periodic pattern with tens of layers of particles. This colloidal crystalline template holds a mixed packing structure called random hexagonal close packing (RHCP) combining face-centered cubic (FCC) and hexagonal close-packed (HCP) yielding the highest packing factor of 0.74, along with a small portion of body-centered cubic (BCC) packing at the center and edge of the spherical pattern.

From the observation, the water evaporation begins once the solution is placed and confined in the cell. Nucleation appears at the very center when the liquid layer is thinned to a critical thickness. Then, the ordered nanosphere multilayer starts to form due to the continuous fluid movement containing particles towards the nucleus. After certain period of time, the ordered region expands out and covers the whole spherical confinement as it dries up. Basically, the strong capillary force developed at a meniscus between a substrate and a colloidal solution brings nanoparticles close to each other forming periodic arrays as the meniscus is slowly swept across a horizontally placed substrate by good control of the evaporation rate of the suspension. The detailed mechanism of 2D crystal formation is explained as follows. At the beginning, a concave shape of the liquid surface of the colloid is formed within the confinement utilizing capillary force resulting from the convex shape of encircling o-ring. When the concave bottom thins to approximately particle diameter, the deformation of the liquid-air interface gives rise to strong inter-particle capillary forces and triggers the nucleation. Then, the crystal grows from the

nucleus by a convective transport of the particles towards nucleus. The further thinning of the concave meniscus water layer between particles in the nucleated region is hindered because of hydrophilicity of the particles. Thus, the hydrodynamic pressure of the water is given risen to carry particles through a convective flow. The evaporation rate of the suspension controlled by the humidity of the surrounding environment plays a crucial role in the self-assembly process. Once humidity is increased in the incubator, the nucleation and crystal growth slows down providing plenty of time for particle to be well positioned. Better quality with fewer defects such as cracks and stacking faults, in this way, can be produced. However, the whole drying process consumes more time. On the other hand, it can also be accelerated in low humidity, but bringing more imperfections to the colloidal crystal.

3.2 Synthesis of Inverse Frustum Nanosphere Gold Arrays

3.2.1 Templated Electrochemical Deposition of Ni and Au

Periodic arrays of gold nonovoid structures are synthesized by electroplating metal from aqueous solution into pre-assembled PS nanosphere templates. The electroplating is performed using a conventional three-electrode cell controlled by a Potentiostat/Galvanostat (Model 273A from Princeton Applied Research). The commercial non-cyanide plating solution (Techni-Gold 25 ES RTU, 0.25 troy/L) is obtained from Technic Inc. The homemade nickel electrolyte contains 0.1 M $NiSO_4 \cdot 6H_2O$, 0.1 M Boric acid and is adjust to PH 3.25 by adding H_2SO_4. [52] The gold coated substrate with colloidal template on it is the working electrode with a platinum mesh counter electrode and a silver/silver chloride reference electrode. Nickel and gold films are deposited under potentiostatic conditions at -0.8 V and -0.6 V versus Ag/AgCl reference electrode (Sat. KCl, 0.197 V vs. Normal Hydrogen Electrode), respectively. The metal ions in the electrolyte are reduced into metal atoms thus forming solid dense smooth film from the conductive gold surface at the very bottom. Different film thickness of the metal nanovoid array structure associated with distinct morphology can be obtained by controlling the passing charges (deposition time). Finally, PS particles are dissolved by sonication (Branson 2510 Ultrasonic Cleaner) in toluene (Alfa Aesar,

Semiconductor Grade, 99% min) for five minutes followed by thoroughly rinsing with IPA and DI water.

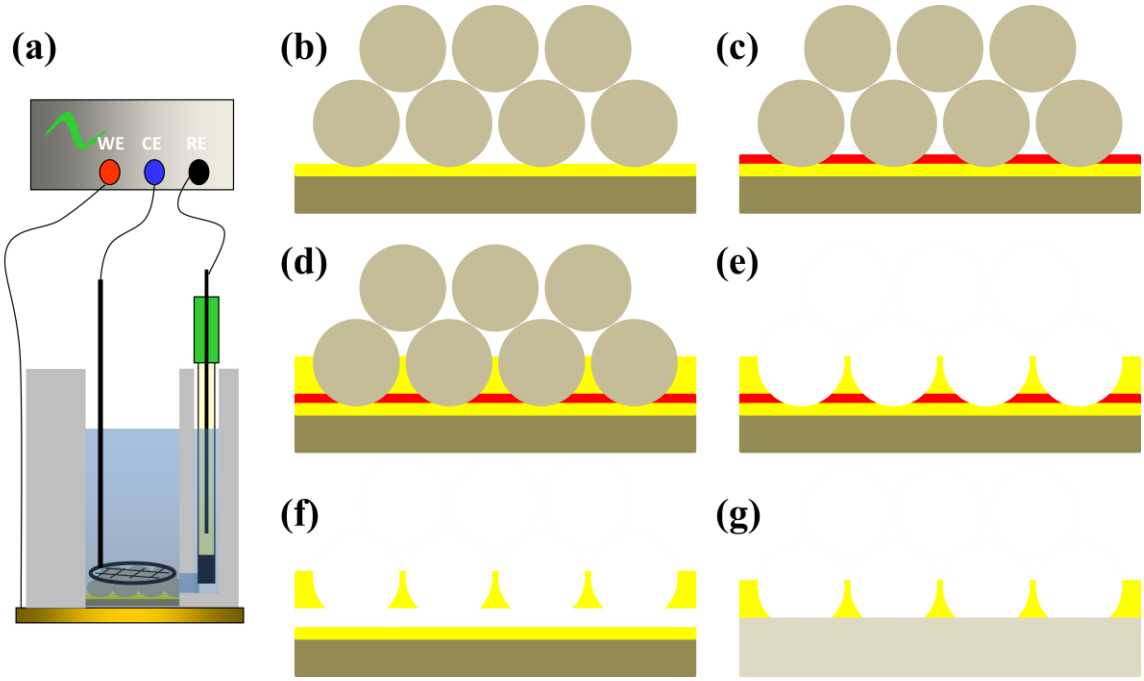

Figure 3-2 (a) Three electrode cell for electroplating (b) ~ (g) Fabrication process of inverse frustum nanosphere gold arrays on cover slip

3.2.2 Etching and Transferring of Gold Films onto Cover Slip

Ni and Au films are deposited into the interstitials of HCP colloid templates consecutively by changing the plating electrolytes without damaging existing patterns for a formation of metallic bilayer structure. After dissolving the template, the metal structure is immersed horizontally into heated nickel etchant (Nickel Etchant TFG, Transene Inc) for thorough etching of Ni layer to release Au layer from substrate. Once the film is lifted and suspended due to surface tension of the liquid, it is gently transferred to DI water for further cleaning. Close attention should be paid to keep the flexible thin film unfolded during the whole process.

To fish out gold film onto the glass cover slip, a cover slip is placed underneath the film, and it is slowly raised out of water. Again, a slow N_2 stream is used to blow away the remaining water on the cover slip to smooth out the film across the whole area without any wrinkles. As a result, gold nanovoid array film firmly stands on the glass surface.

The deposited nickel layer serves as a sacrificial layer for two purposes. First, since it is impossible to manufacture such structure on a needle size fiber cross-section surface, certain transferring technique is required for moving fabricated film from large substrate to small spots. Etching of nickel layer brings this idea into reality and can be expanded to transferring to any flat surfaces. The biggest advantage of integrating optical fiber with this plasmonic structure is that it enables in situ and in vivo sensing without traditional sampling which could result in less timely and accurate information. Second, it creates uniform spherical bottom openings for each void embedded in the gold film. Better yet, the size of the hole can be well controlled by manipulation of nickel layer thickness by changing the deposition time. The longer deposition time is, the thicker the nickel layer will be, and the larger diameter of the bottom opening will be. In this structure, bottom hole adjacent to fiber tip is for introduction of incident light and collection of the reflected light while the front opening is for interrogation of analyte molecules inside the voids. Without the openings at the bottom, it is not possible to obtain the enhanced electrical field inside the voids when light from a fiber is incident on the bottom surface of the arrays. Also, it is not possible to spontaneously pass the light, both incoming and reflecting, in the same fiber. A lot of papers have reported the sensing properties of nanovoid array structures, but without openings the bottom. In that case, a reflection setup is used where light source is usually presented above the front opening together with a separate detector. Analyte solution has to be sampled out and spread all over the structured substrate on the stage for sensing. Both incoming and outgoing light is inevitably affected by aqueous solution, leading to the variation of experimental results. In a word, our unique design works perfectly for developing a high efficiency fiber plasmonic sensor for in situ and in vivo sensing applications.[53]

The new inverse frustum nanosphere structure is similar to cylindrical nanohole arrays embedded in an Au film. But the fabrication process of the inverse frustum nanosphere array structures is simple, inexpensive, and scalable, capable of generating large areas of samples in parallel at a low cost, while cylindrical-hole arrays are typically produced by conventional lithographic process, which requires several microfabrication steps using complex equipments.

3.3 Optical Measurements

Fig. 3-3 illustrates the homemade set up for characterizing the optical fiber tip LSPR sensor based on spectra reflection. The light source is a broadband (350 nm to 1100 nm) Tungsten Halogen lamp. The light is coupled into a single mode optical fiber (105 μm diameter, 0.22 NA, Thorlab Inc) and directed to a 50:50 beam splitter via a collimating lens. The beam splitter transmits half of the light to a focusing objective lens and the light is coupled again to the fiber with gold nanovoid arrays on the tip surface. The fiber and objective lens also collect and pass the reflected light back to the beam splitter which directs it to a focusing lens followed by a fiber and finally, the light is detected by a USB-4000 spectrometer (Ocean optics Inc).

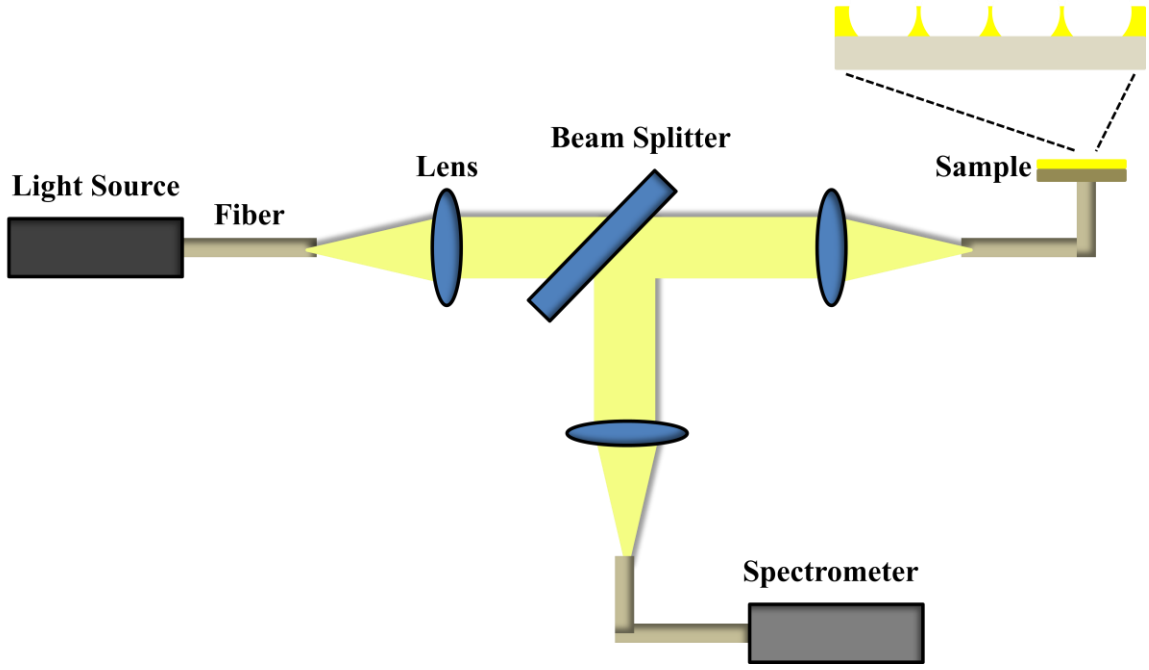

Figure 3-3 Home made optical fiber based UV/VIS spectrometer in reflection configuration

To get a reference reflection spectrum, an optical fiber is stripped, cleaved and covered with a thin silver film as a reflection mirror. The dark spectrum is obtained by connecting a fiber without any coating on the tip surface with the source light on when the room light is turned off. The measured reflection spectra (R) of the fiber tip LSPR sensor probe is calculated by the following equation:

$$R = \frac{I_S - I_D}{I_R - I_D} \times 100\% \qquad (3\text{-}1)$$

where I_S is the sample intensity over white light range, I_D is the native dark spectrum by fiber, I_R is the reference spectrum by silver mirror. Each reflectance spectrum is taken with 60 ms integration time for 3 times.

3.4 Finite Difference Time Domain (FDTD) Simulation

For the computational study of optical properties of inverse frustum nanosphere arrays, FDTD method is utilized to solve Maxwell equations all across the structure under illumination of the white light. The commercial software, Lumerical FDTD solutions 7.5, provides a good and simple interface for design, analysis and optimization of nanophotonic devices.

First, a square piece of SiO_2 is placed in the working space with a gold thin film (thickness ranging from 100 nm to 500 nm) on it. Then truncated sphere close packed arrays (n side = 3) with diameter from 300 nm to 1000 nm are embedded within the gold film. Same periodic arrays of cylinders (100 nm to 300 nm wide) are structured adjacent to SiO_2 surface at the bottom center of each sphere. All the spheres and cylinders share the same refractive index with environment (i.e.1.00 as air, 1.33 as water). To simulate the molecule binding events on the surface, a very thin layer (less than 5 nm) of dielectric medium is evenly distributed for studying the sensing behavior of reflection based LSPR sensor.

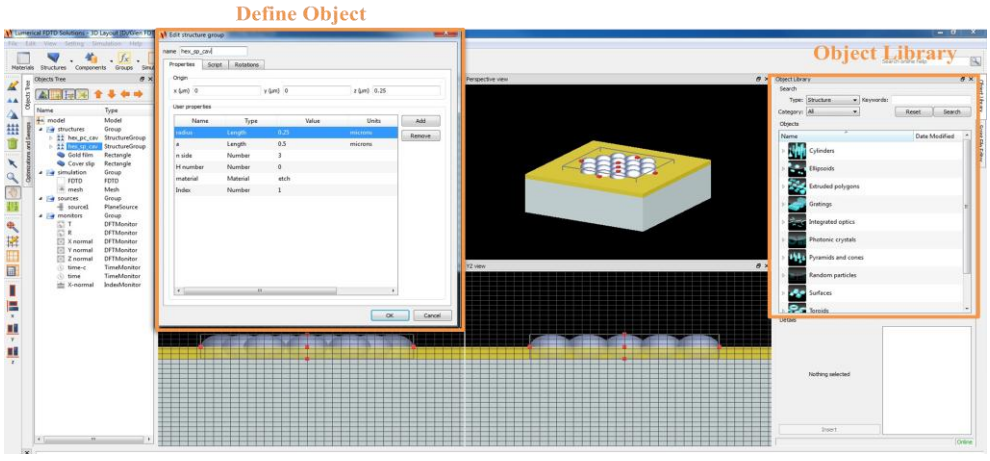

Figure 3-4 Create physical structure

Second, the simulation region is set slightly larger than nanovoid-array area with upper boundary fairly above tip surface and lower boundary below it. Periodic boundary condition is applied. A mesh with a grid unit of 5 nm × 4.33 nm × 5 nm is spread all over the gold film region to create repeatability of mesh points in each sphere.

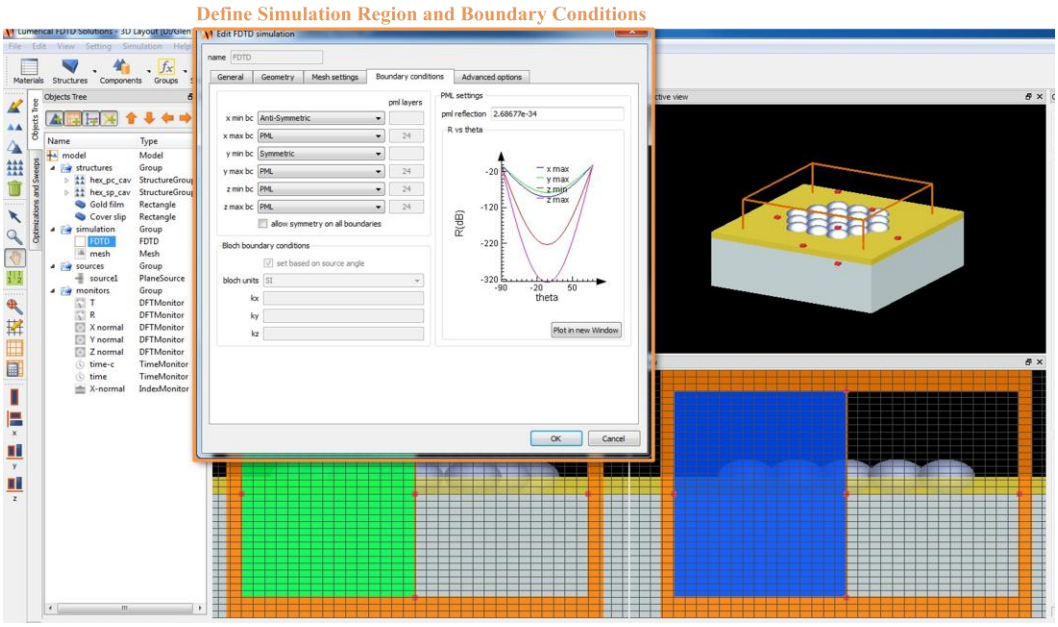

Figure 3-5 Define simulation region and boundary conditions

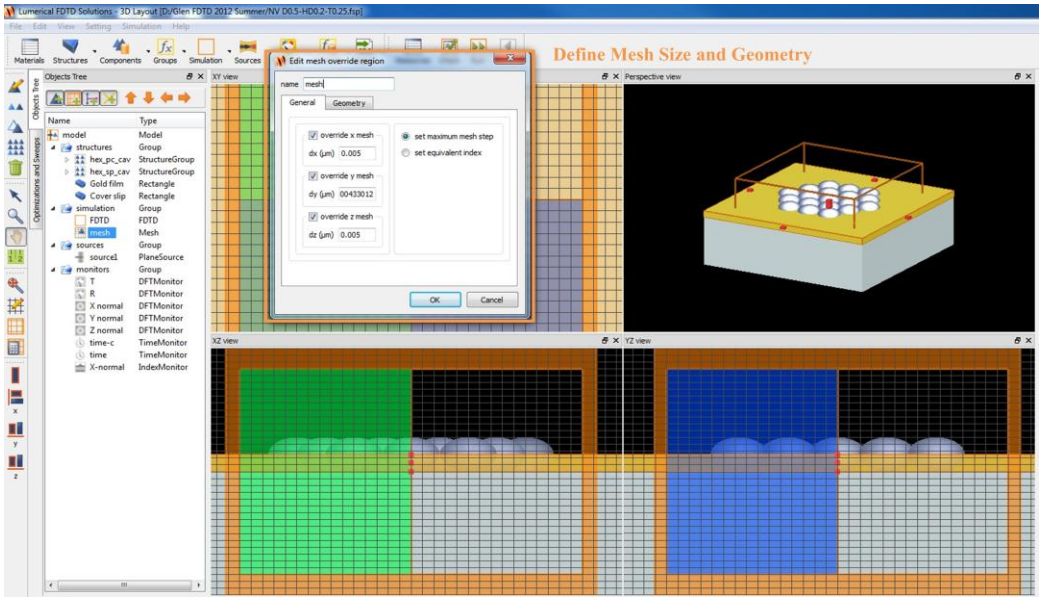

Figure 3-6 Define mesh size and geometry

Third, a square-shape plane wave source slightly larger than simulation region in x-y plane with wavelength from 400 nm to 1000 nm is defined and placed horizontally underneath the gold film within the simulation region so that light is injected vertically to the bottom surface of the gold film forward z-axis.

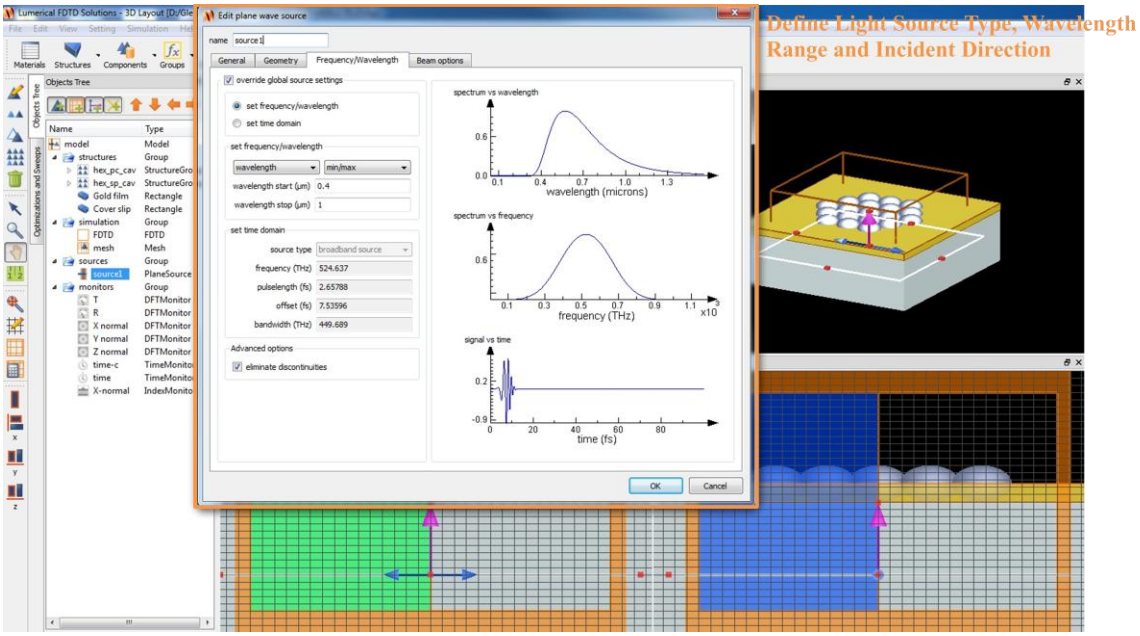

Figure 3-7 Define light source type, wavelength range and incident direction

Fourth, two frequency-domain field and power monitors are plotted on front and back side of the gold nanovoid arrays for transmission and reflection measurements respectively. The detection range is same as the source, electromagnetic fields and power data are recorded. In addition, a frequency domain profile monitor is inserted into the arrays across the center of one of the spheres parallel to z axis while another is configured slightly above one of the voids parallel to x-y plane for investigation of electric field strength profile inside the void.

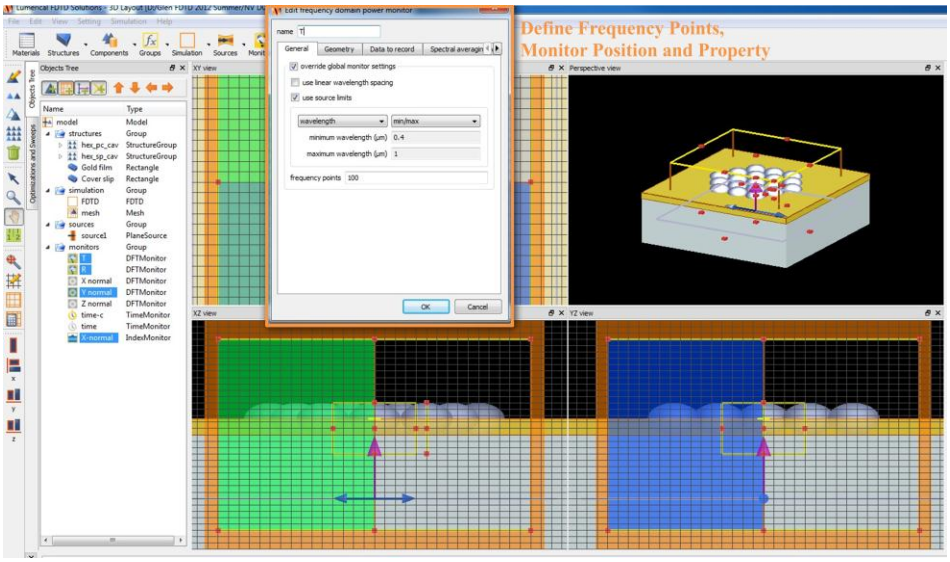

Figure 3-8 Define frequency points, monitor position and properties

Finally, after running the simulation, reflection and transmission spectra can be obtained spontaneously by applying scripting language to the data stored in two frequency-domain field and power monitors. Also, electric field intensity distribution information can be pulled out from the frequency domain profile monitors by correctly selecting resonant frequency/wavelength of specified structure from previous reflection/transmission spectra.

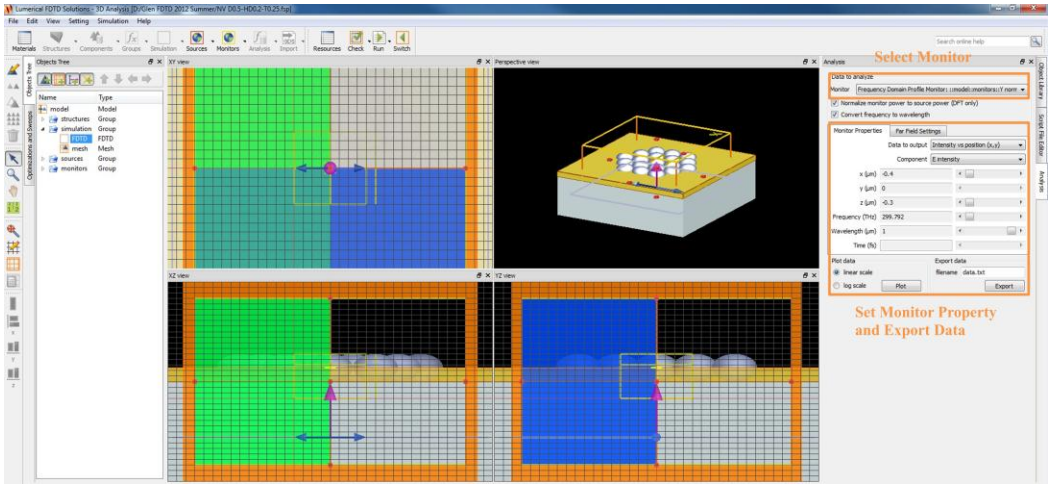

Figure 3-9 Select monitor, define monitor property and export data for analysis

CHAPTER 4

RESULTS AND DISCUSSION

In this chapter, the fabrications of self-assembled polystyrene nanosphere templates and inverse gold frustum nanosphere arrays are first discussed. Then, experimental and simulated reflection spectra of inverse gold frustum nanosphere arrays with different morphology are compared and discussed. After that, factor sweeps are performed in FDTD solutions in order to find out the relation between LSPR peak and structural parameters. At last, preliminary results are shown to explore potential application as molecule sensor.

4.1 Assembly of Templates and Electroplating

Figure 4-1 shows the crystal structure of assembled polystyrene templates with different particle sizes. Particles, less than 1 micron, are close packed in a hexagonal manner with multiple layers. Most of the crystals are in RHCP structure, but small portion of BCC crystal can be found near the edge of the samples. Small amount of defects such as vacancies, grain boundaries was observed. Although, a lot of methods have been proposed to produce high quality colloidal crystals which are free of defects microscopically, our technique, which utilizes strong capillary force sweeping across the sample due to controlled solvent evaporation turns out to be a simple and effective approach. We found that the high quality templates can only be assembled on Au (Au film coated substrate) surface. Other metal surfaces such as Cu, Ni and Ag have been tried, but the templates formed on these surfaces suffer a much poorer periodicity or even completely randomness.

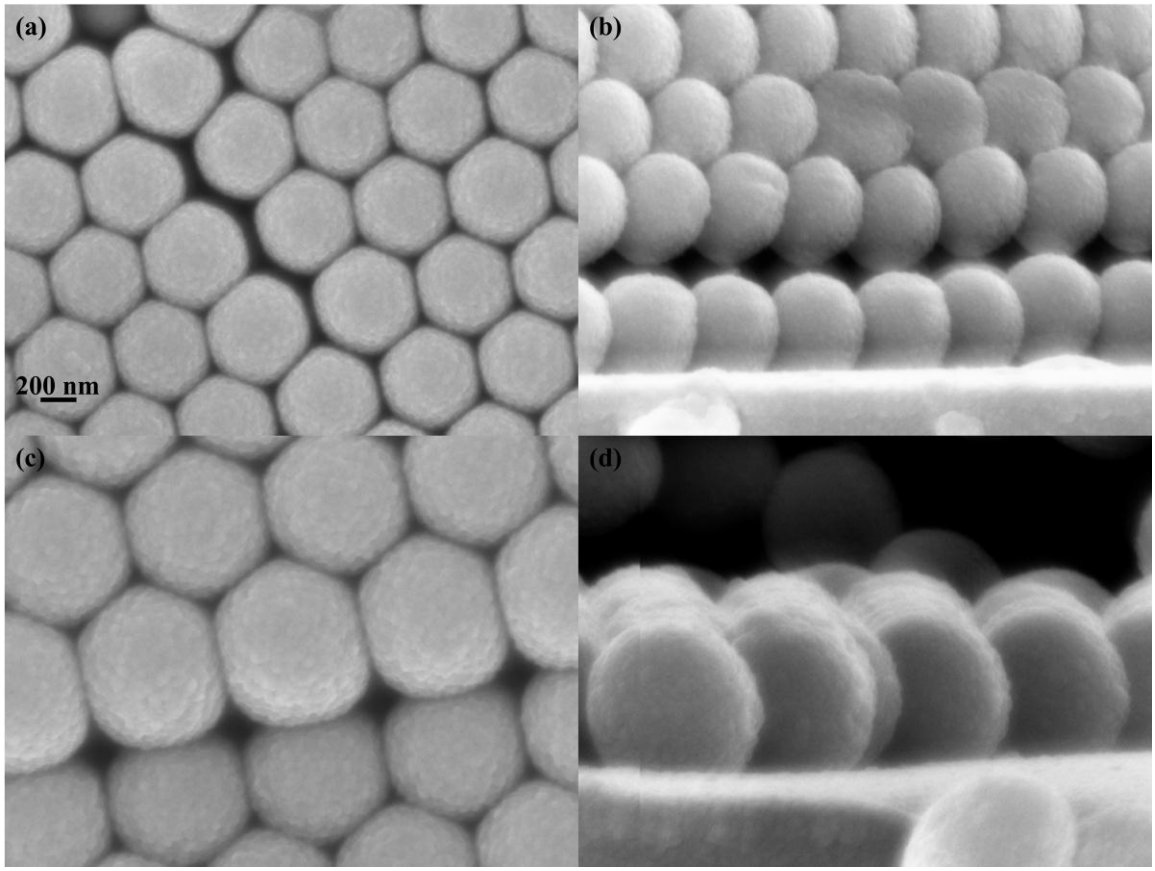

Figure 4-1 (a) (b) Plane/Cross-section view of 500 nm template (c) (d) Plane/Cross-section view of 750 nm

Metal films such as gold and nickel were electro-deposited into the templates. Usually, film thickness is controlled by electro-deposition charge (time) to be around the radius of the template particle into the very bottom layer. As a result, such “lost wax” process will leave us well arranged circular openings on the top of gold film. A field emission high resolution scanning electron microscope (Zeiss-Supra 55VP) was used to capture images for study of microstructure of the templates and subsequent metal films. The SEM images show smooth and uniform openings with hexagonal packing. The center to center distance between two neighboring pores is the same as the diameter of the polystyrene particle which is used for self assembly. As expected, the metal film with embedded dimples is true cast of the template.

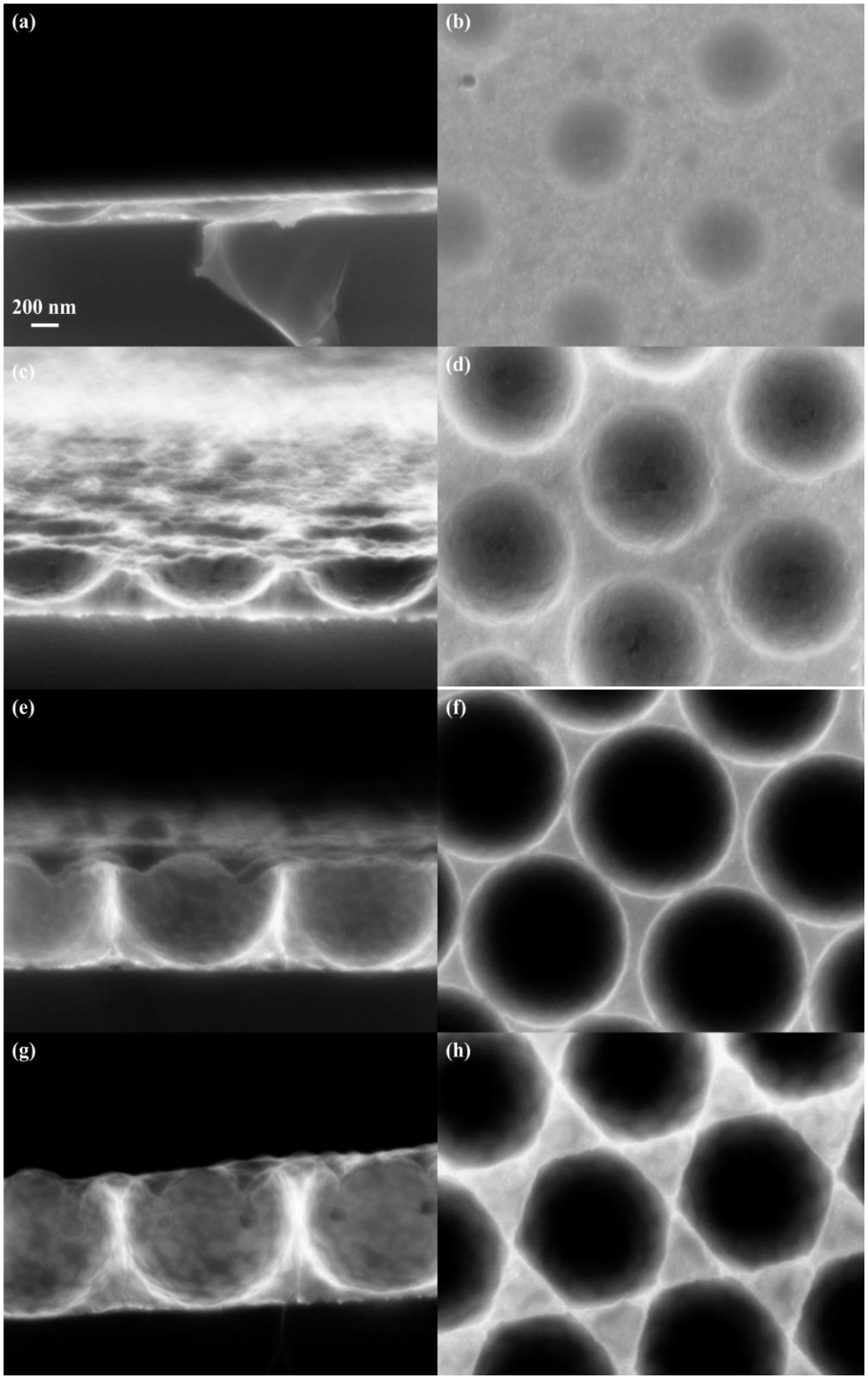

Figure 4-2 (a) (c) (e) (g) Cross-section view of nanostructure with continuously increasing thickness fabricated from 750 nm template (b) (d) (f) (h) Corresponding plane views

By applying trigonometry knowledge, the relation between film thickness and pore mouth size is easily calculated as

$$t = r \pm \sqrt{r^2 - r_{pore}{}^2} \qquad (4\text{-}1)$$

where t is the film thickness, which can be measured by cross-section SEM image, r is the radius of the sphere and r_{pore} is the radius of the pore, which can be measured by plain-view SEM image. With continuous film growth shown in Fig. 4-2, the pore size will reach a maximum when t is equal to the radius of the template particle. If the film deposited close to the thickness of the bottom first layer of polystyrene particles, it will reach the spheres of the second layer. As a result, it will block the diffusion of the metal ion to grow flat surface and this accounts for the hexagon shape mouth instead of circular shape ones.[52, 54] The match of the calculated value and measured value of pore size is another good proof for the feasibility of such templated electroplating.

4.2 Plasmonic Properties of Gold Inverse Frustum Nanosphere Arrays

4.2.1 Surface Plasmon Resonance of Gold Inverse Frustum Nanosphere Arrays

The gold film with embedded periodic cavities has been widely studied by researchers and scientists in terms of different plasmon modes it supported. Generally, when gold film is thin (less than the radius of the template sphere), the nanostructured surfaces take the form of a thin two dimensional grating. Such diffractive coupling, which also takes effect in prism and grating, refers to “Bragg plasmon”. [55] When gold film is thick (around the diameter of the template sphere), the surface structure takes the form of spherical cavities. The electromagnetic solutions to individual spherical dielectric cavity within an infinite expanse of metal correspond to “Mie plasmon” from a sphere.[56] This plasmon mode can be schematically described by One bouce/Two bouce model referring to interference effect due to travelling path difference of reflected light ray.[55, 57] The energy of Bragg modes varies according to incident and azimuthal angles, while Mie plasmon energy is thickness dependent.

Since the sample thickness we fabricated is pretty thin, Bragg plasmon modes dominate in surface plasmon resonance. The hexagonally arranged voids act as a phase matching tool to generate a six-fold diffraction pattern as illustrated in Fig. 4-3. The in-plane wave vector can be modified as [58, 59]

$$K_z = k\sin\theta + g_{pq} \tag{4-2}$$

$$g_{pq} = pA + qB \tag{4-3}$$

$$A = 2\pi(b \times n)/|a \times b| \tag{4-4}$$

$$B = 2\pi(n \times a)/|a \times b| \tag{4-5}$$

where a, b and A, B are primitive vectors of 2D lattice and its reciprocal lattice respectively. SPR is excited when wave vector k matches the propagation constant of SPP, in which $K_{SP} = \frac{\omega}{c}\sqrt{\frac{\varepsilon\varepsilon_m}{\varepsilon+\varepsilon_m}}$.

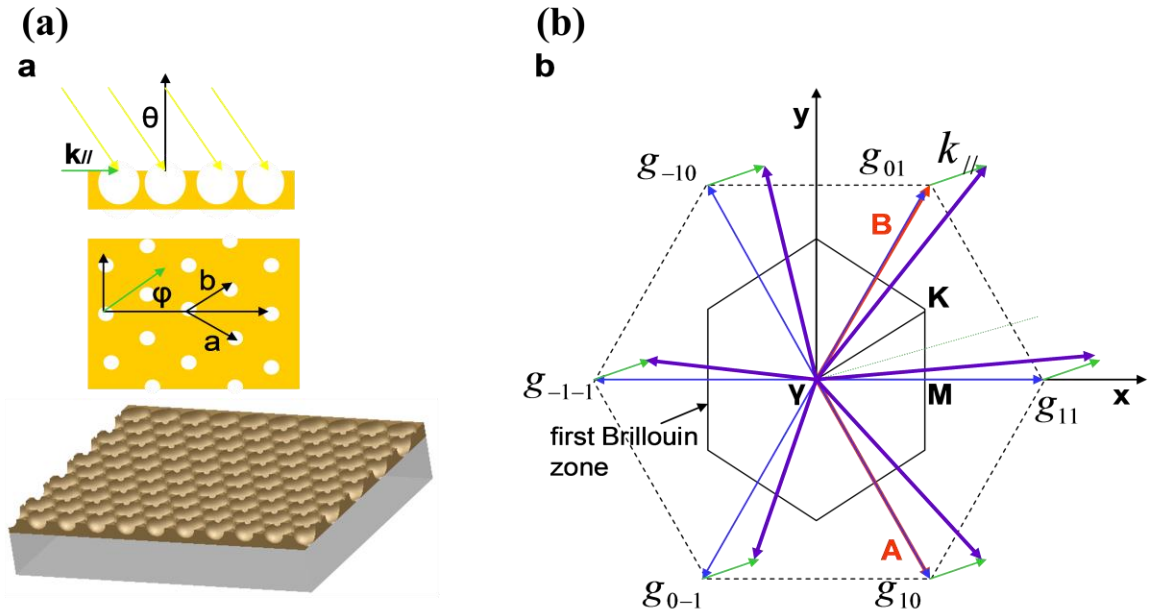

Figure 4-3 (a) Illustration of nanovoid structure with light incident with a tilt angle θ and azimuthal angle ψ (b) Modified of wave vector due to grating effect

As a result, SPR is displayed as an intensity drop in a reflection spectrum, where the surface plasmon resonant frequency of the structure can be identified at the corresponding wavelength/frequency. In a traditional reflection measurement where an objective lens is placed above the sample stage to collect both incoming and outgoing light, the reflection spectra of a plane gold film and a gold film with periodic frustum spherical voids with same thickness (about radius of the template particles) are obtained. At shorter wavelength (below 500 nm), regardless of sample structure, violet light is strongly absorbed due to interband transition of gold metal. At longer wavelength (red/near infrared region), when measuring solid gold film, the reflectance remains constantly high which indicates that SPR is not supported in flat gold film. It is explained that the wave vector of surface plasmon at gold/air interface always lies outside the light cone of air in a dispersion curve. In contrast, dip appears in case of nanostructured gold film because modified surface acts as phase matching tool to bring overlapping between those two wave vectors.

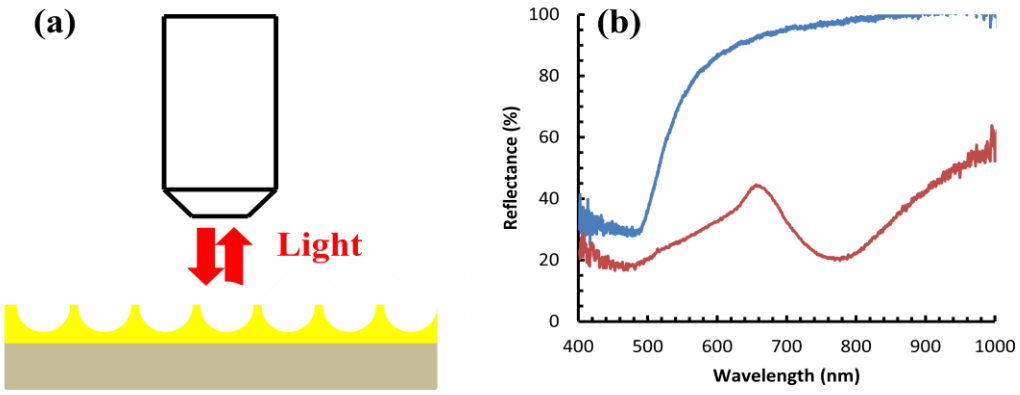

Figure 4-4 (a) Reflectance measurement of nanovoid structure in a traditional set up (b) Reflectivity of gold nanostructure with LSPR (red) and plane gold film with no LSPR (blue)

4.2.2 Redesign of Au Frustum Nanovoid Arrays for Fiber-based Probe Sensing Applications

Needing to note, plasmonic effect can be easily observed in a typical reflection measurement as mentioned above. However, for sensing or SERS application, it requires sampling of analytic solution and placing the sample between detector and plasmonic substrate. The efficiency is largely reduced due to the penetration of the light through the solution to the

substrate surface. Thus, in order to make it into a signal amplifier fiber probe for in situ and in vivo sensing, a new measurement setup is designed as mentioned in previous chapter. In this setup, light is introduced and collected from backside of substrate with analytic solution on the front side. Unfortunately, as shown in Fig. 4-5 (b), no LSPR peak appears in this measurement, just like plane gold film. This demonstrates that even a very thin layer of gold film used for self assembly (around 10 nm) can totally prevent the light from coupling with nanostructure to ignite LSPR.

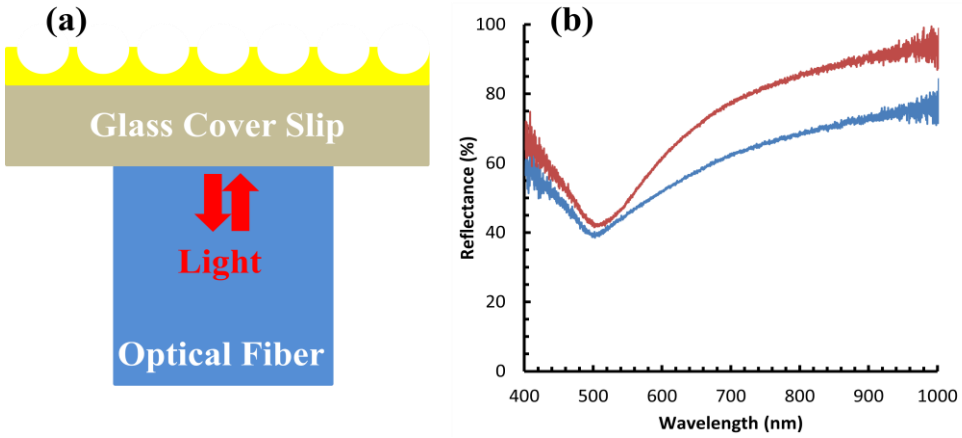

Figure 4-5 (a) Reflectance measurement of gold nanostructure in homemade UV/VIS spectrometer (b) Reflectivity of gold nanostructure with no LSPR (blue) and plane gold film with no LSPR (red)

To better understand this phenomenon, we systematically study the effect of pre-coated gold film thickness on excitation of LSPR by changing bottom Au film thickness in FDTD simulation. Closed packed nanovoid arrays with sphere diameter of 500 nm and electroplated film thickness of 250 nm in air and water environment are simulated.

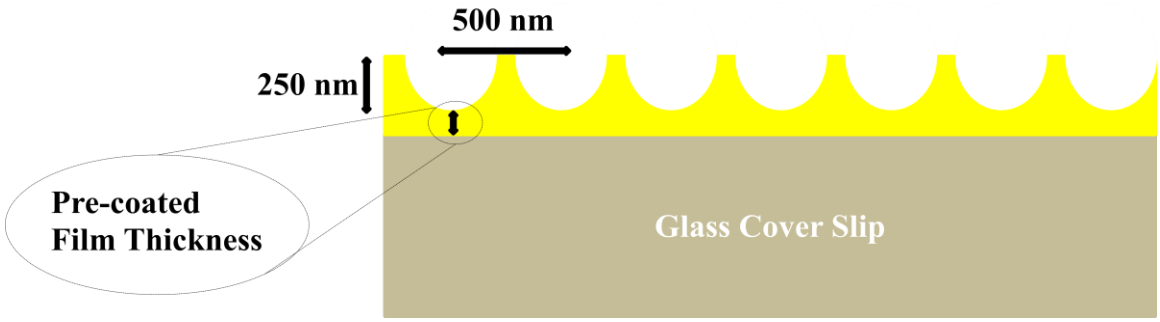

Figure 4-6 Sketch of inverse frustum nanosphere arrays with variable pre-coated gold film thickness in FDTD simulation

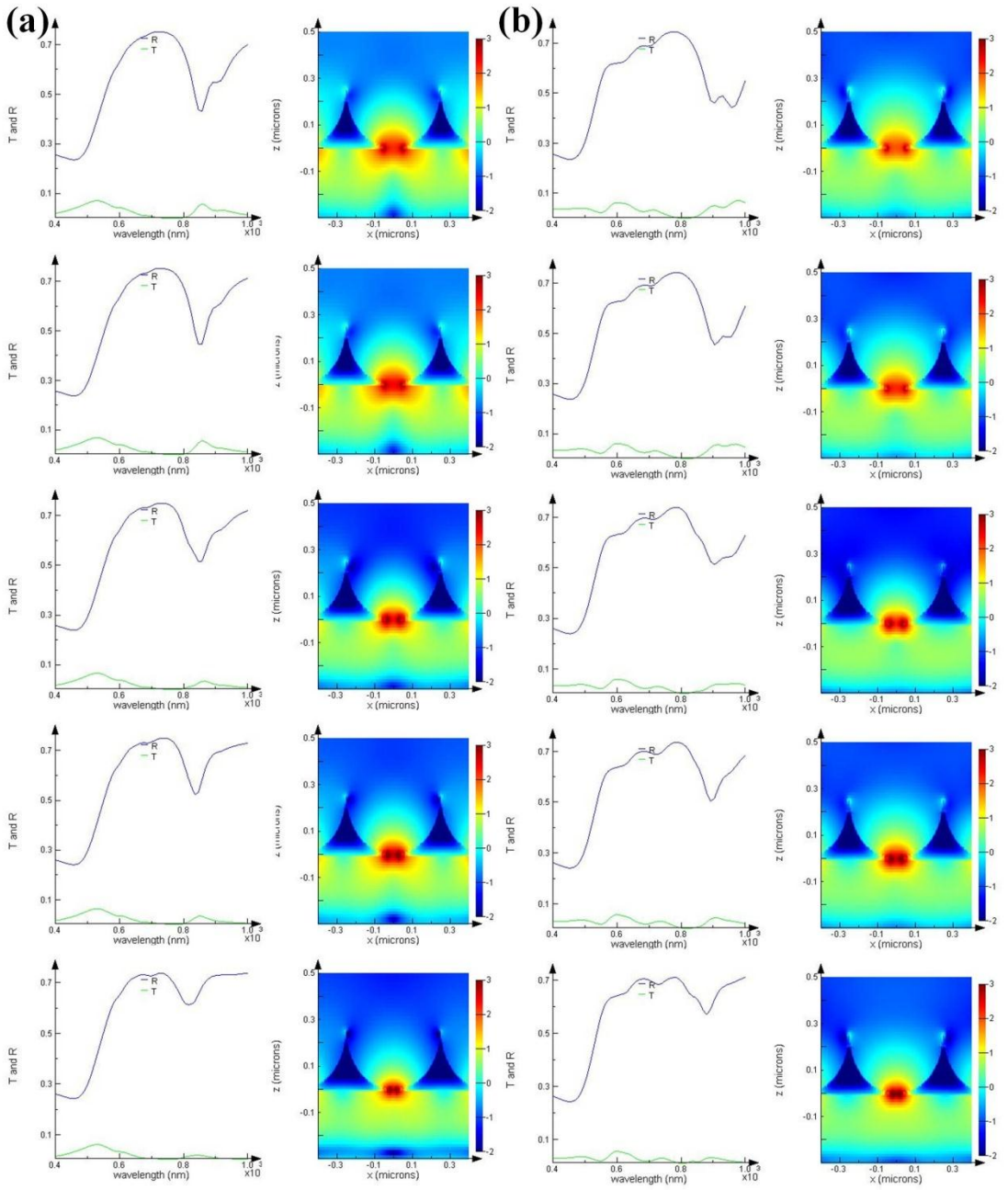

Figure 4-7 (a) Reflectance spectra and electric field distribution of gold nanostructure with pre-coated gold film thickness of 0, 1, 2, 3, 4 nm from top to bottom in air condition (b) Reflectance spectra and electric field distribution of gold nanostructure with pre-coated gold film thickness of 0, 1, 2, 3, 4 nm from top to bottom in water condition

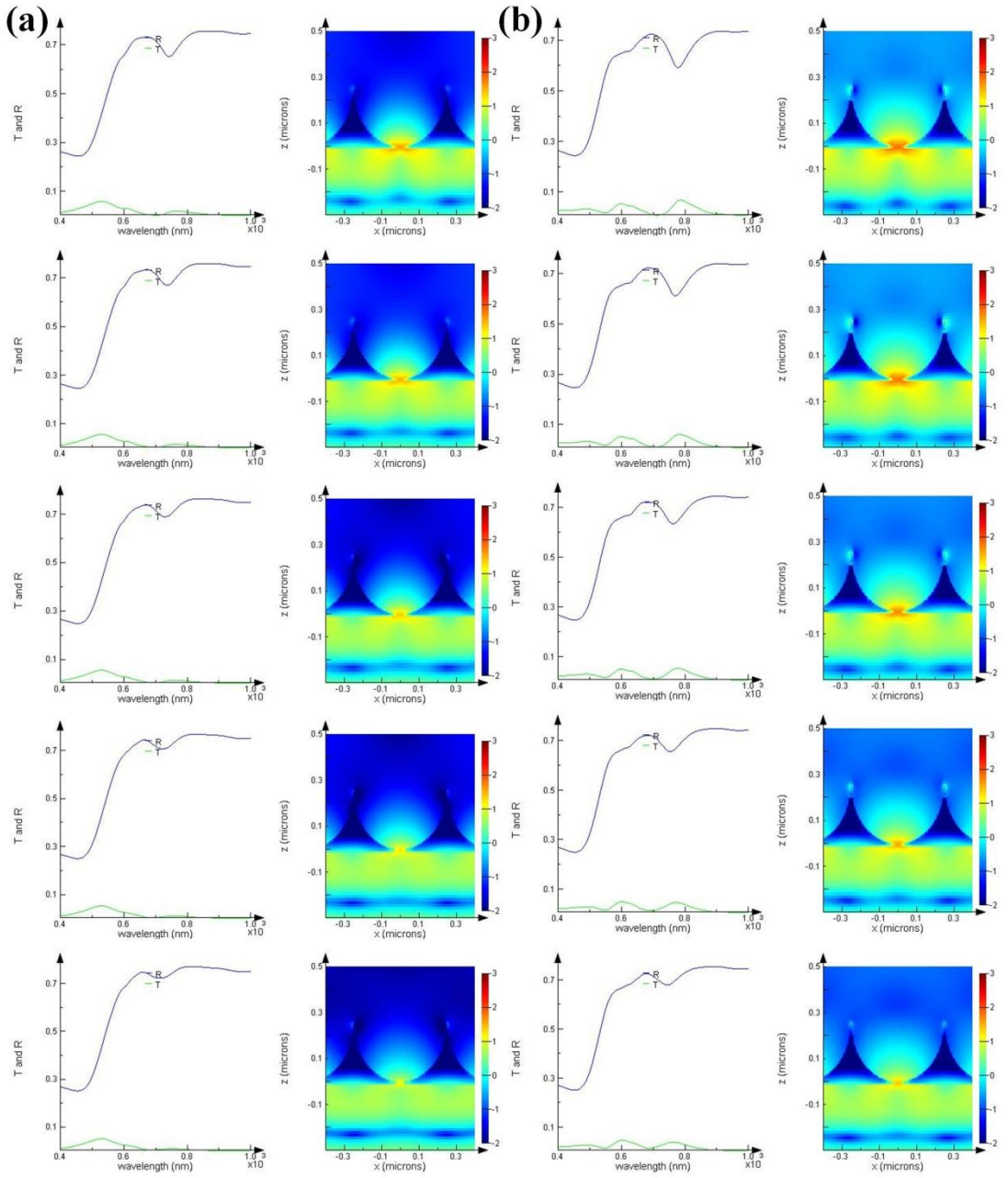

Figure 4-8 (a) Reflectance spectra and electric field distribution of gold nanostructure with pre-coated gold film thickness of 5, 6, 7, 8, 9 nm from top to bottom in air condition (b) Reflectance spectra and electric field distribution of gold nanostructure with pre-coated gold film thickness of 5, 6, 7, 8, 9 nm from top to bottom in water condition

When pre-coated gold layer is less than 4 nm thick, the plasmonic structures show clear peaks at the wavelength around 840 nm in air and 900 nm in water. That yields a sensitivity of

180nm/RIU. “Hot spot” region where electric field is dramatically enhanced exists at the bottom of each spherical void and expands up to 70 nm at both front and back sides. The strongest electric field (most red spots) presents as a circle radiating outwards at the gold/dielectric interface with a fixed distance from gold/glass interface. As gold thickness grows, the circle almost collides into one point at thickness of 4 nm which leads to the shrinkage of “hot spot” region. When pre-coated gold film keeps increasing (larger than 4 nm), the LSPR peaks become unacceptably shallow and finally vanish, the reflection curve flats out at around 10 nm. Meanwhile, electric field intensity drops significantly and enhancement vanishes as well. We come up with the conclusion that the critical thickness of pre-coated gold film is 4 nm. And it is a good verification and explanation for the blackout of LSPR in previous samples.

In reality, it is almost impossible to fabricate continuous and dense metal film as thin as 4 nm by physical vapor deposition, so a new structure is designed where circular opening is created at the bottom of each void for light indicence and collection. The feasibility of this unique design is first demonstrated by FDTD simulation of the structures with cylindrical bottom holes of diameter of 150 nm. A narrow and deep LSPR peak is successfully achieved as well as enhanced electric field at the bottom of each void. Experimentally, such modified structure can be realized by introducing a sacrificial nickel layer with controllable thickness as mentioned in details in previous chapter. The LSPR peak offers a convincing evidence to support the practicability and advantage of this creative design.

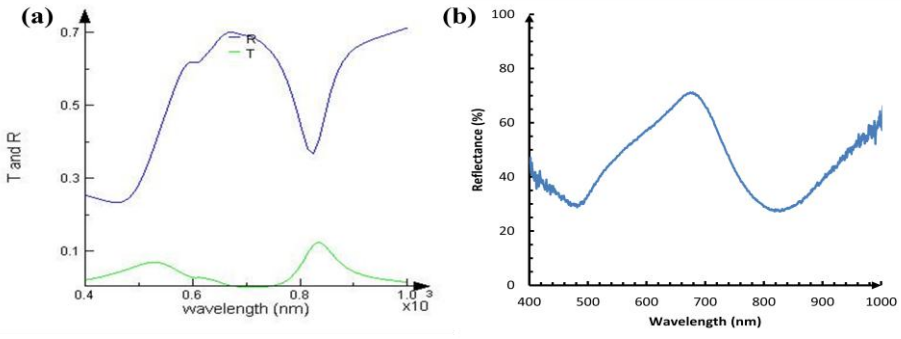

Figure 4-9 (a) Reflectance spectrum of gold nanovoid structure with bottom opening of 150 nm in diameter in FDTD simulation (b) Reflectance spectrum of fabricated structure by introducing a Ni sacrificial layer to create bottom openings

4.2.3 Structure Parameters of Au Frustum Nanovoid Arrays with Bottom Openings and LSPR

In this session, redesigned nanovoid structures with different structure parameters including film thickness and bottom opening size using 505 nm PS templates are studied with FDTD simulation and their dielectric sensing performance (from air to water) and tunablility of LSPR wavelength/frequency are experimentally evaluated.

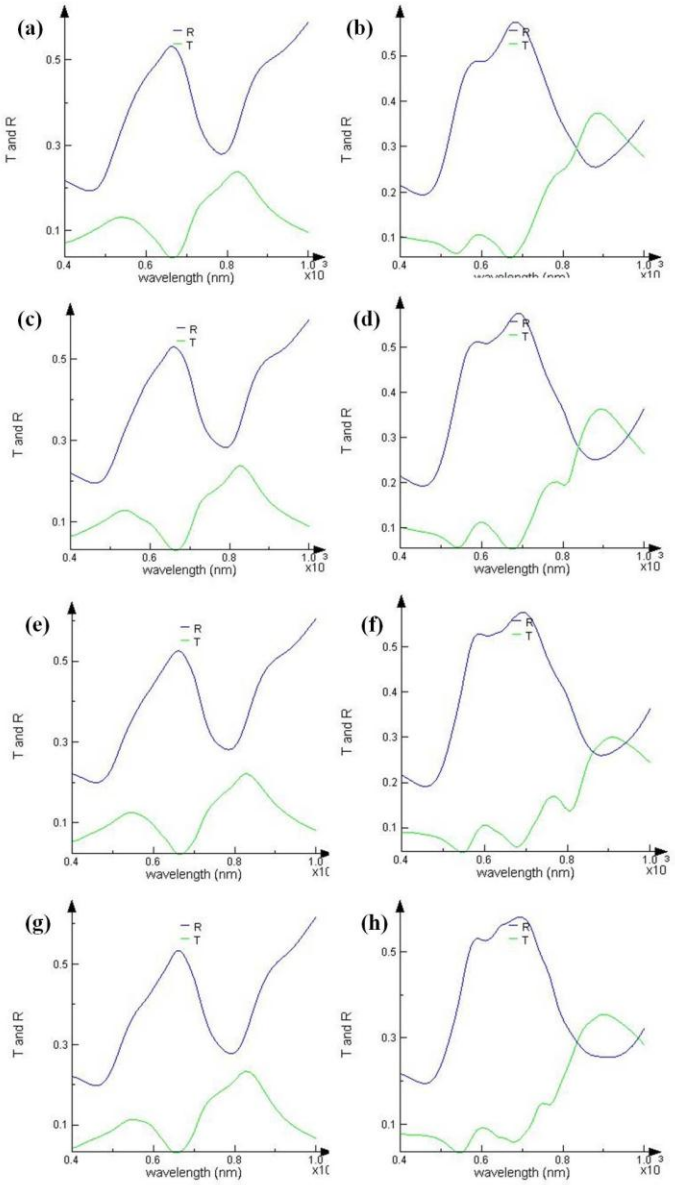

Figure 4-10 (a) (c) (e) (g) Reflectance spectra of gold nanostructure with bottom opening of 320 nm in diameter and 200 nm, 240 nm, 300 nm and 340 nm in film thickness from top to bottom in air condition in FDTD simulation (b) (d) (f) (h) Corresponding reflectance spectra in water condition

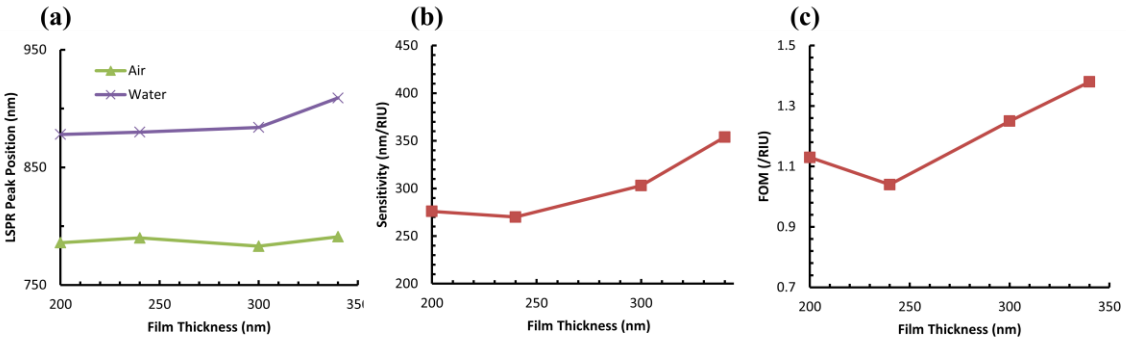

Figure 4-11 (a) LSPR wavelength in water and air condition (b) Sensitivity with variation of film thickness (c) Figure of Merit with variation of film thickness

First, we study the effect of gold film thickness on LSPR peaks. The simulation results come from a perfect void array with uniform front opening, bottom hole and film thickness as shown in Fig. 4-17 (b) and summarized in Fig. 4-11. The bottom hole diameter is fixed at 320 nm and different film thicknesses are picked at 200 nm, 240 nm, 300 nm, 340 nm. Two dielectric conditions, air (n=1) and water (n=1.33), are compared. In this case, as bottom hole increases, the LSPR peak position, in another word, LSPR wavelength in air condition is nearly the same at about 785 nm, and it slightly increases in water condition from 880 nm to 910 nm. Overall, the sensitivity and Figure of Merit, which is sensitivity divided by resonance band width, become higher, reaching to 350 nm/RIU and 1.38/RIU, respectively.

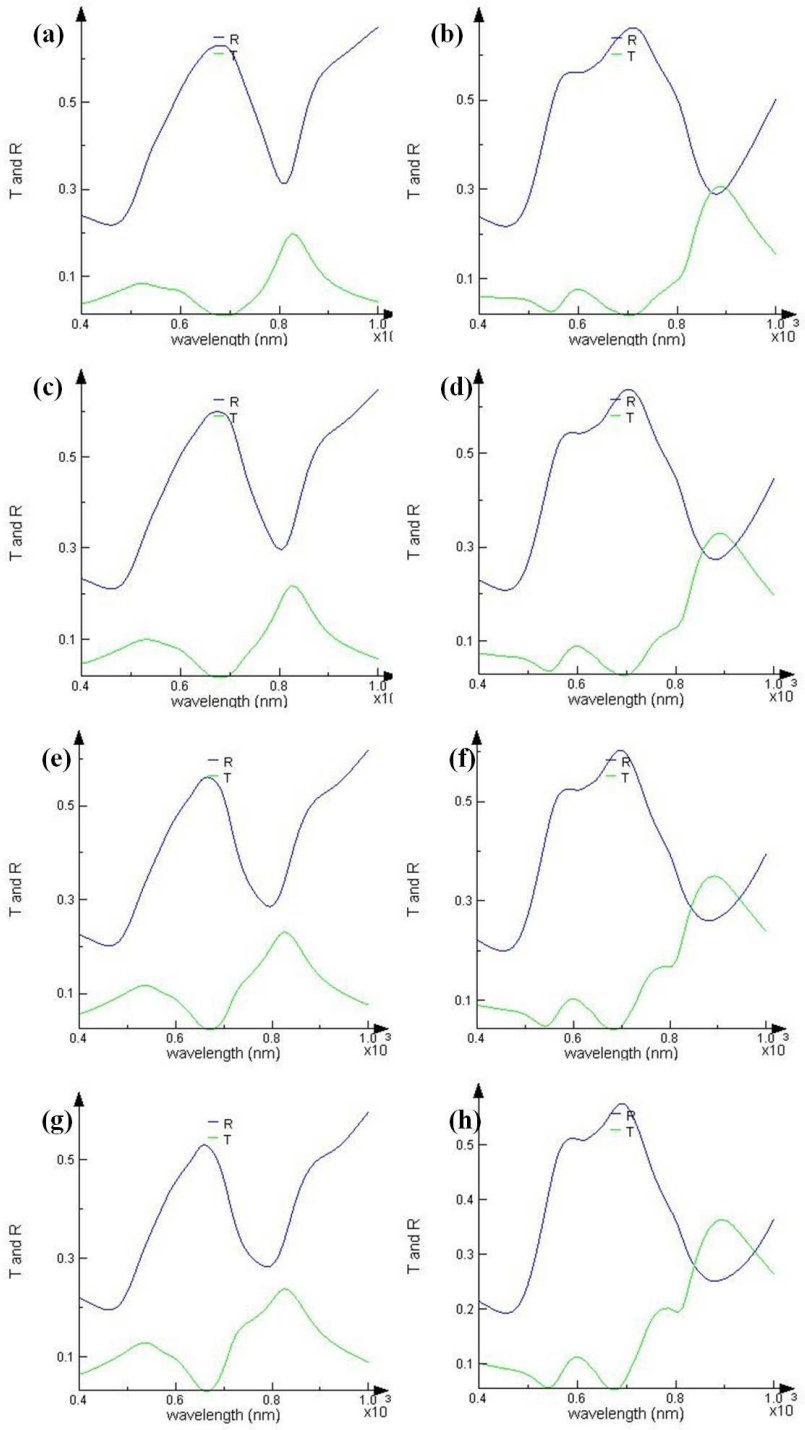

Figure 4-12 (a) (c) (e) (g) Reflectance spectra of gold nanostructure with film thickness of 240nm and 240 nm, 270 nm, 300 nm and 320 nm in bottom hole diameter from top to bottom in air condition in FDTD simulation (b) (d) (f) (h) Corresponding reflectance spectra in water condition

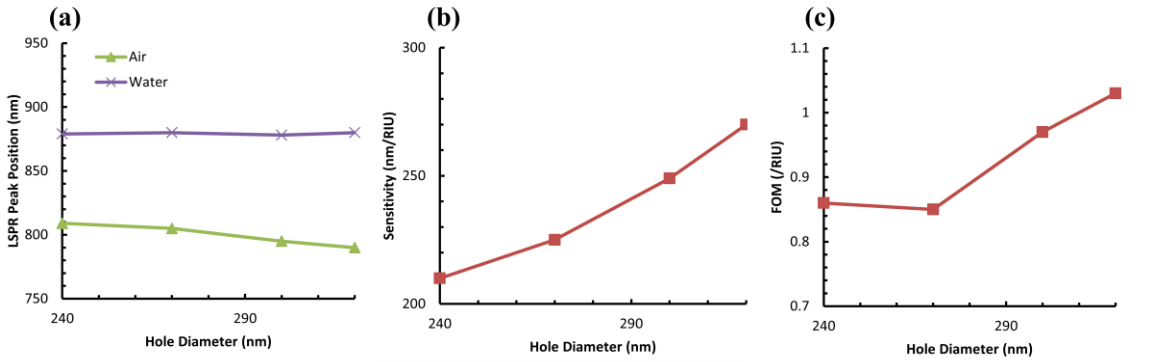

Figure 4-13 (a) LSPR wavelength in water and air condition (b) Sensitivity with variation of bottom hole diameter (c) Figure of Merit with variation of bottom hole diameter

Second, we study the effect of bottom hole size on LSPR wavelengths for gold nanostructures with Au film thickness of 240 nm for 505 nm template. Samples with bottom hole diameter of 240 nm, 270 nm, 300 nm, 320 nm are picked up for simulation. The results are summarized in Fig. 4-13. As bottom hole expands, LSPR wavelength in air slightly blue-shifts around 800 nm while it remains the same at 880 nm in water. Thus, the resulting sensitivity increases from 210nm/RIU to 270nm/RIU and FOM increases from 0.86 to 1.03.

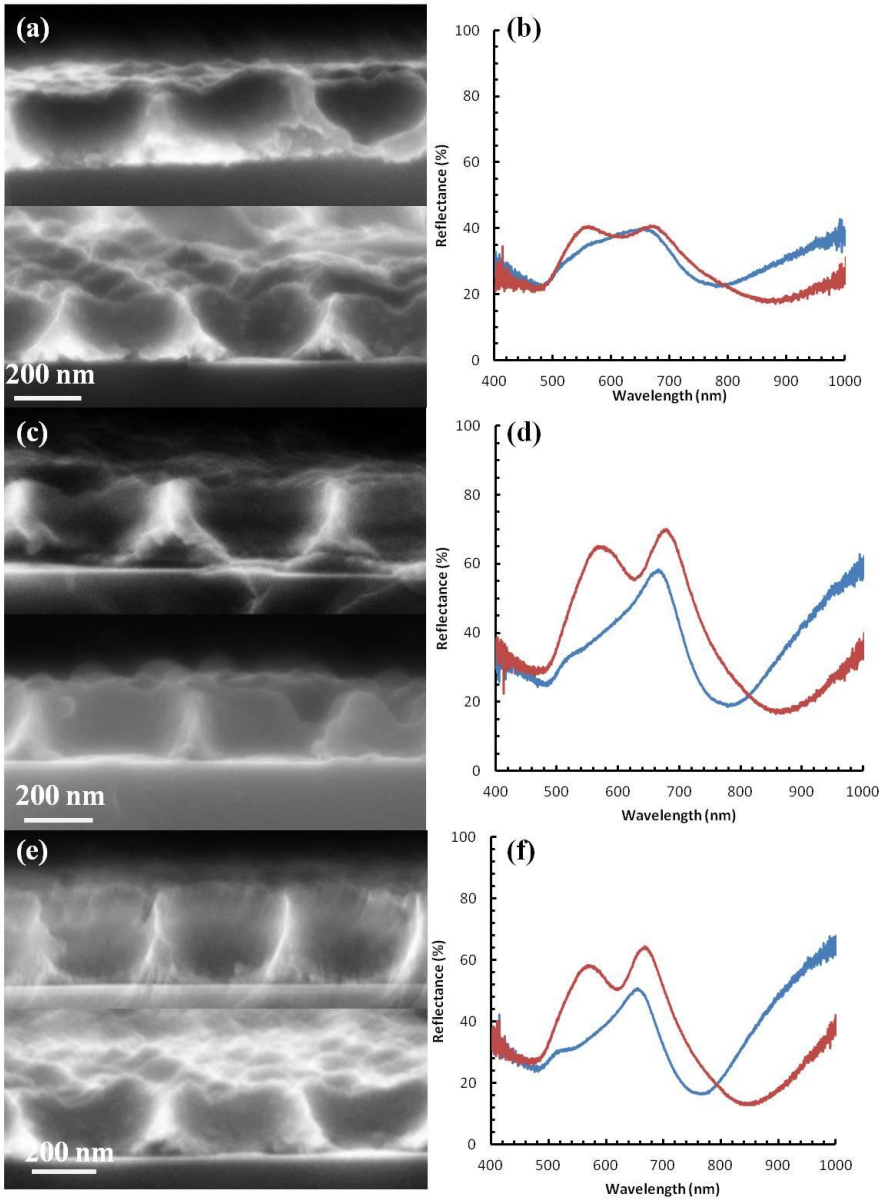

Figure 4-14 (a) (c) (e) SEM images of gold nanostructures before and after etching with a bottom opening diameter of 320 nm and 200 nm, 240 nm, 285 nm in film thickness from top to bottom (b) (d) (f) Corresponding reflectance spectra showing LSPR wavelength shift from air (blue) to water (red)

Since the diameter of the circular bottom opening is determined by the thickness of electroplated Ni layer,

$$t - t_{Au} = r - \sqrt{r^2 - r_{BO}{}^2} \qquad (4\text{-}6)$$

where t and t_{Au} are film thickness before and after etching of Ni layer which can be measured by cross-section SEM image, r and r_{BO} are the radius of template sphere and bottom opening. For example, a Ni/Au metal film with thickness of 50 nm and 200 nm using template sphere of 505 nm in diameter will have a bottom opening of 300 nm in diameter.

To verify the simulated results, we fabricated the structures with film thickness and bottom hole diameter and measured their LSPR wavelengths. From calculation, a Ni layer with thickness of 60 nm will produce a circular bottom hole with diameter of 320 nm. A series of nanostructures with theoretically uniform bottom hole and varied gold film thickness is produced and shown above. The bottom hole diameter is around 320 nm and film thickness is around 200 nm, 240 nm, 285 nm respectively. Meantime, another series of nanostructures with film thickness at 240 nm and different bottom hole diameter at 240 nm, 270 nm, 300 nm, 320 nm are studied as below. These samples are measured in a homemade UV/VIS spectrometer. In this setup, a small PDMS pool is placed to encircle and hold deionized water on top of gold films for measurement of reflectance in water condition.

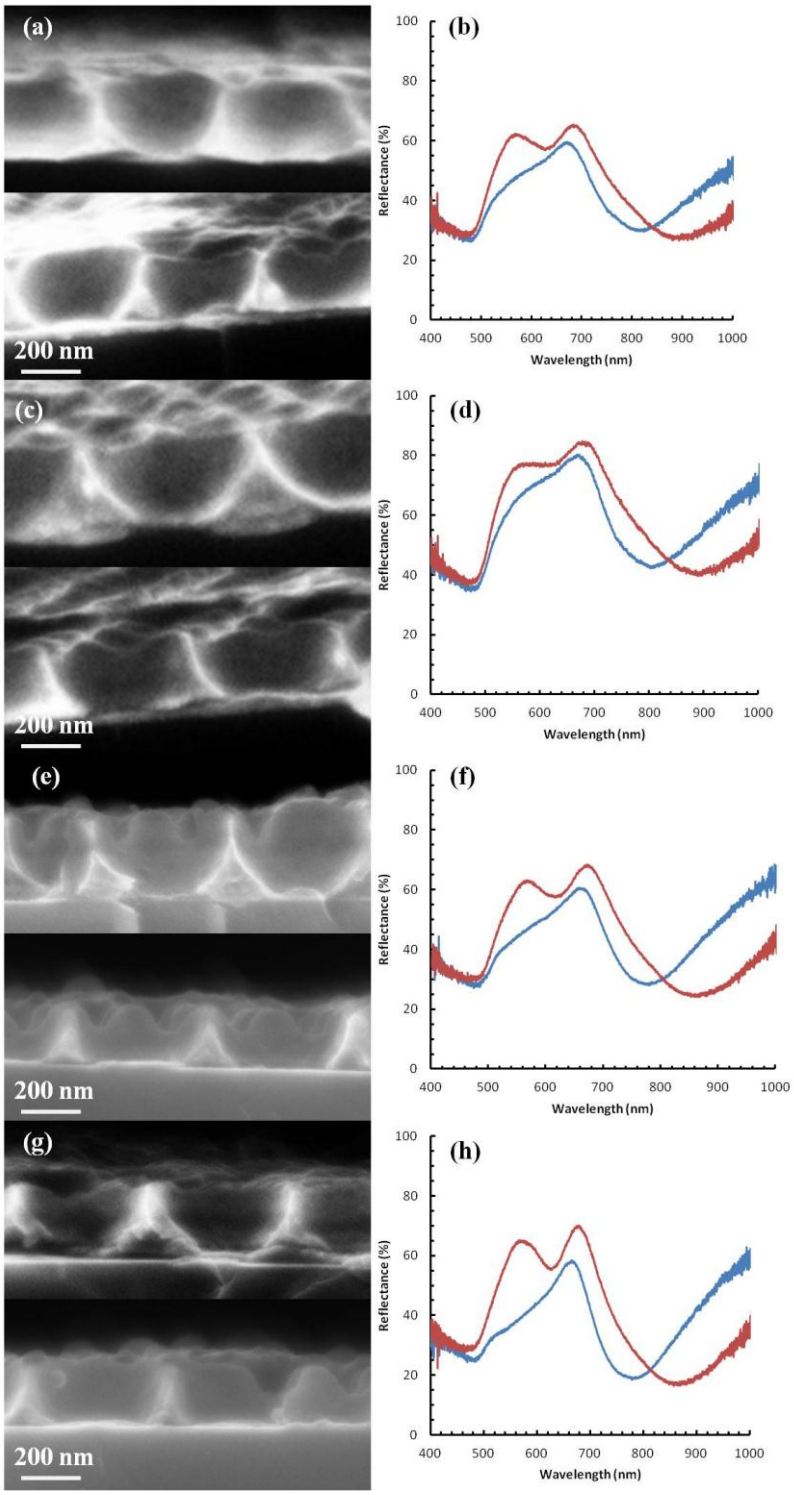

Figure 4-15 (a) (c) (e) (g) SEM images of gold nanostructures before and after etching with a film thickness of 240 nm and 240 nm, 270 nm, 300 nm and 320nm in bottom hole diameter from top to bottom (b) (d) (f) (g) Corresponding reflectance spectra showing LSPR wavelength shift from air (blue) to water (red)

It can be seen that there is a deviation in LSPR position, sensitivity and figure of merit between experiment and simulation data. Since gold deposition begins from the bottom where the largest available area is, it requires longer time to grow certain thickness of gold which means the thickness is more controllable. Later on, the deposition area shrinks and growth of gold film accelerates which makes manipulation of thickness very difficult. Also, as mentioned before, the PS layer on top of bottom layer affects the uniform diffusion of gold ion and generates some preferential sites for deposition as shown in Fig. 4-16 (a). Once the thickness exceeds half sphere of PS sphere, complex structure appears and it accounts for different plasmon modes in sensing behavior.

The measured resonance peak is always broader. It can be explained in following aspects. Optical fiber works based on total internal reflection, thus, the incident light is not exactly normal and multiple phase matching condition can be realized in different wavelengths. Also, the template quality is not uniform from the fabrication process. Besides the PS particle size deviation of about 20 nm, template stacking plays a crucial role. Vacancies, dislocations, grain boundaries, uneven nanosphere sitting position will all lead to lack of uniformity or even loss of bottom holes as illustrated in Fig. 4-16 (b).

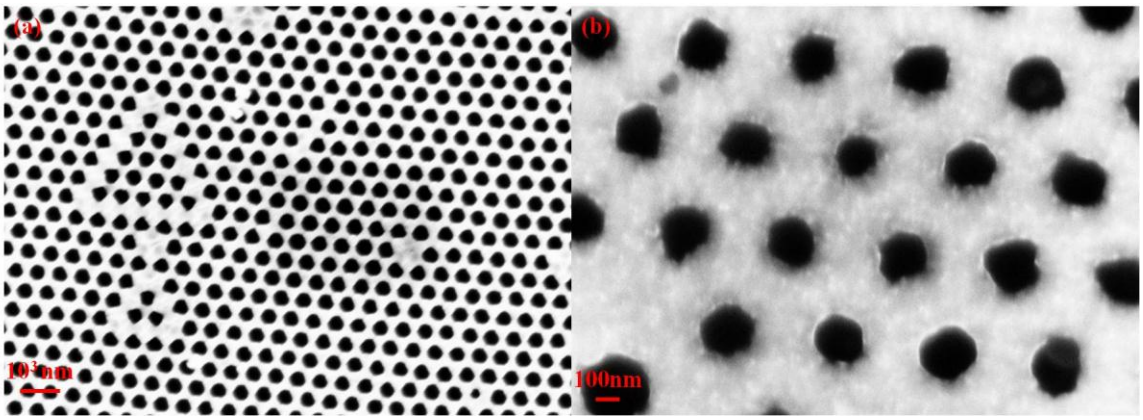

Figure 4-16 (a) SEM image of plane view of gold nanovoid structure showing preferential film growth and complex structure (b) SEM image showing bottom opening distribution taken after gold film is released and flipped over

4.2.4 Advantages of Inverse Frustum Nanosphere Gold Arrays as Plasmonic Sensor

In previous section, the effect of different structure parameters of gold inverse frustum nanosphere arrays on its plasmonic property has been studied in experiments and simulations. Cylindrical hole arrays have been studied and reported by many researchers for its plasmonic property. Here, by using Lumerical FDTD solutions 7.5 again, sensing property of gold cylindrical hole arrays and our gold inverse frustum nanosphere arrays are compared, and certain analysis and conclusion are made. At the end, the potential application as molecule sensor of this gold nanovoid arrays is predicted as well.

As seen in Fig. 4-17 (a) (b), cylindrical hole and nanovoid arrays with same periodicity (hexagonal packing, separation distance 500 nm), varied film thickness (50 nm, 150 nm, 250 nm) and bottom hole diameter (50 nm, 100 nm, 150 nm, 200 nm) in same environment change (from air to water) are compared. Needing to note, the former has one hole size as independent variable regardless of film thickness while the front opening size is correlated to the film thickness. Again, LSPR wavelength in air and water, along with sensitivity are simulated.

For frustum sphere arrays (FS), LSPR peak in air shifts to shorter wavelength as hole diameter increases, while cylindrical hole (CH) shifts to longer wavelength. FS experiences a maximum in LSPR peak in water at the hole diameter of 100 nm, while CH remains the same trend as in air. Also, there is a minimum hole diameter (around 150 nm) for CH to excite LSPR. FS is more film thickness-irrelevant as resonance wavelength shifts a little when film thickness varies, while CH is largely film thickness-dependent, where LSPR blue shifts as the film becomes thinner. Also, CH experiences a cap for the thickness at around 250 nm above which LSPR vanishes. As a result, the sensitivity of FS is better than CH in general and is less restricted to structure. In summary, FS outplays CH in dielectric sensing with better sensitivity and more structurally flexibility. This is because more “hot spot” region is generated in FS than CH due to high aspect ratio of this innovative design of nanovoid arrays with bottom holes. Meantime, in CH, film thickness, hole diameter are interdependent and altogether have to be small and large enough to excite LSPR and “hot spot” region.

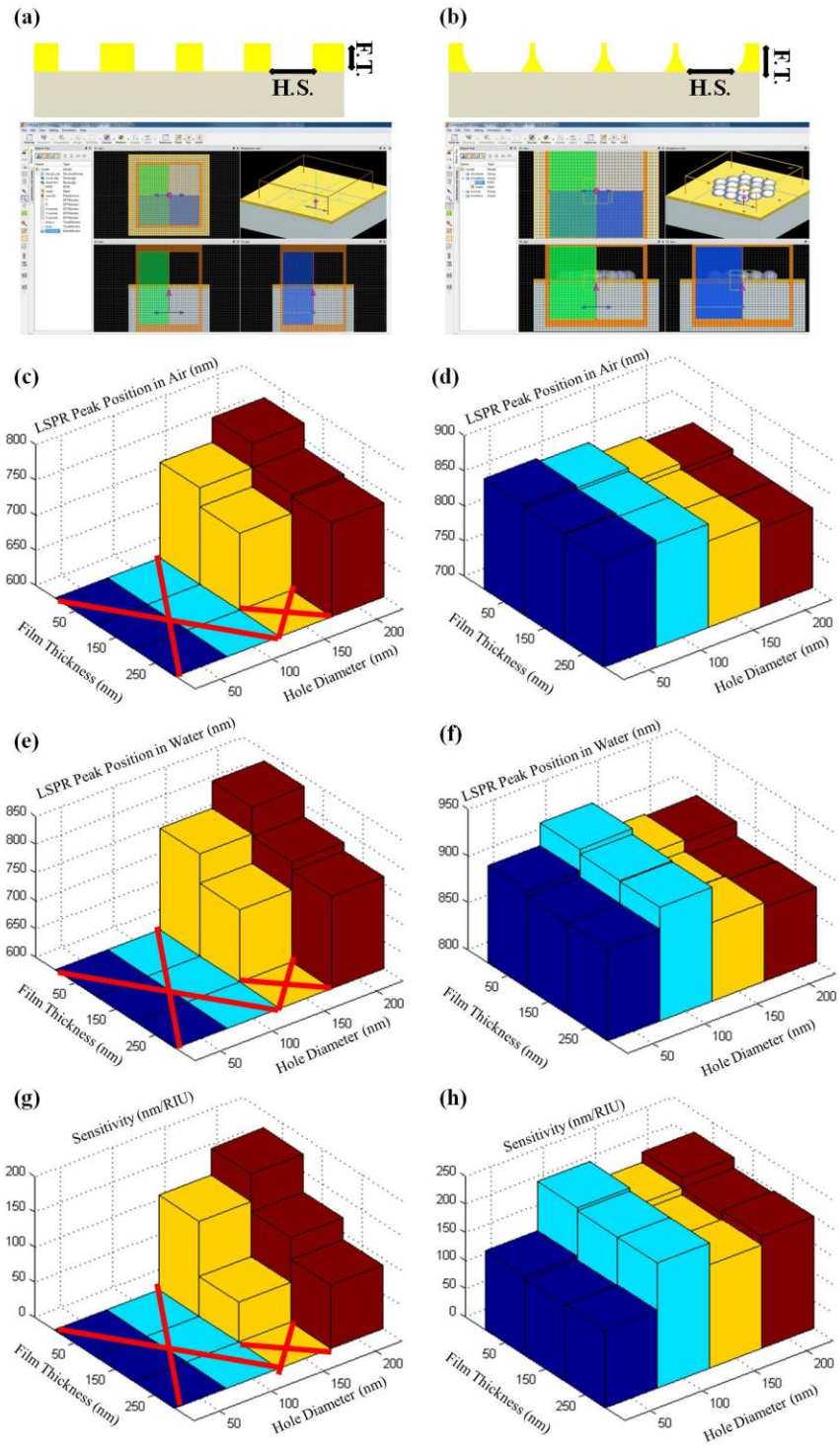

Figure 4-17 (a) (b) Sketches of cylindrical hole arrays and inverse frustum nanosphere arrays in FDTD simulation (c) (e) (g) The effect of film thickness and bottom hole diameter on LSPR wavelength in air/water, and resulted sensitivity for cylindrical hole arrays (d) (f) (h) The effect of film thickness and bottom hole diameter on LSPR wavelength in air/water, and resulted sensitivity for inverse frustum nanosphere arrays

4.2.5 Simulation of Bio-molecule Sensing Application

LSPR has been reported in recent years for its ability to detect molecular adsorption such as polymers, DNA or protein, etc. The mechanism of detection is based on that the adsorbing molecules give rise to changes of local refractive index, thus change of resonance condition of surface plasmon waves. As illustrated in Fig. 4-18, we model this scenario with a 5 nm dielectric layer attached to our nanovoid arrays in an original water environment. By continuously changing the refractive index of dielectric layer from 1.4 to 1.7, the change of resonance wavelength is monitored and plotted. In the plot, the slope of the curve represents the sensitivity of about 40nm/RIU, which is pretty low. The mesh size (δx = 5 nm, δy = 4.33012 nm, δz = 5 nm) really affects the results for a 5 nm layer, but smaller mesh size will cost both time and more computer resources. Thus, once the thickness is increased to 25 nm, the sensitivity boosts to 135nm/RIU. The potential application of inverse frustum nanosphere gold arrays as molecule sensor is predicted and demonstrated.

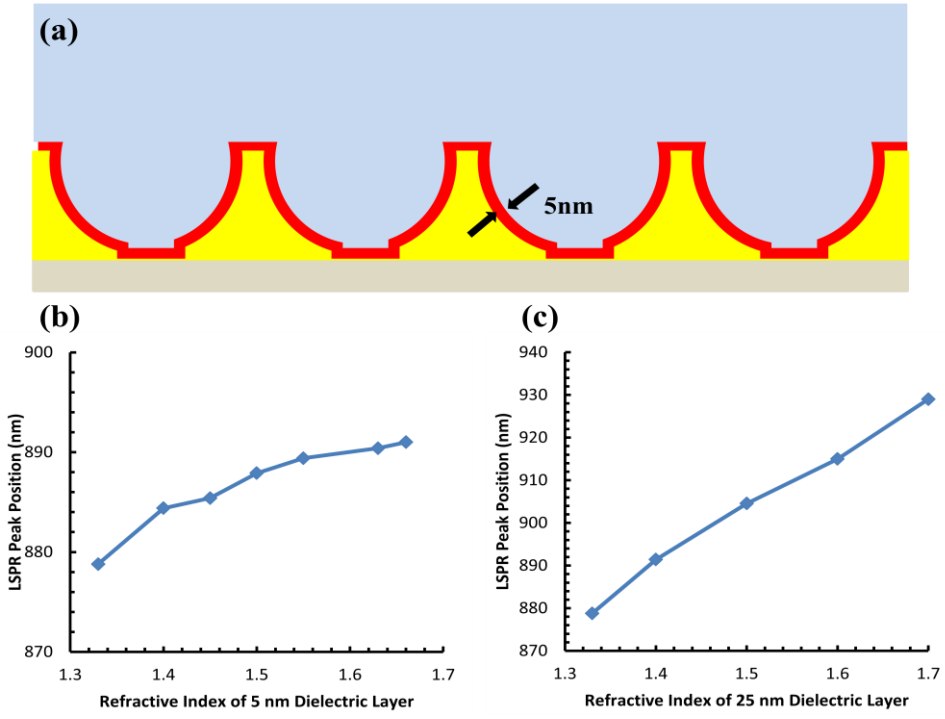

Figure 4-18 (a) Sketch of inverse frustum nanosphere arrays with a 5 nm thin dielectric layer adsorbed on the surface in water environment in FDTD simulation (b) The effect of refractive index change of a 5 nm thin layer on LSPR wavelength (c) The effect of refractive index change of a 25 nm thin layer on LSPR wavelength

CHAPTER 5

CONCLUSION

A multilayer polystyrene colloidal crystal template is self-assembled in a physical confinement by means of capillary force and convective flow. The microspheres are periodically stacked in a random hexagonal close packed (RHCP) structure with certain amount of defects including vacancies and grain boundaries.

The feasibility of electro-deposition into spacing between particles in the template for fabrication of inverse frustum nanosphere gold arrays with controllable structure is demonstrated. Such structure is highly plasmonic active due to its periodic nanostructures. In this structure, the excited SPP propagating at the interface of dielectric/ metal interface is sensitive to local refractive index change which will generate a shift of LSPR wavelength in its reflection spectrum.

In order to develop a portal optical fiber probe for in situ and in vivo biosensing, a modified inverse frustum nanosphere gold array structure has been designed, where circular opening is created at the bottom of each hemispherical void. The plasmonic property of this new design is first investigated by FDTD simulation and then realized by electrodepositing a sacrificial nickel layer underneath the gold layer.

The effect of morphology of the structure including bottom hole diameter and film thickness in a 500 nm sphere template on plasmonic property is studied experimentally, and the results are compared with simulation data. Using computer simulation, the sensing ability using modified inverse frustum nanosphere gold array structure is proved.

Cylindrical hole arrays and our unique structures are studied parallelly with various structural parameters by FDTD simulation. Inverse frustum sphere arrays outperform cylindrical hole arrays for higher sensitivity and more structure flexibility.

REFERENCES

1. Barnes, W.L., A. Dereux, and T.W. Ebbesen, Surface plasmon subwavelength optics. Nature, 2003. 424(6950): p. 824-830.
2. Krasavin, A.V., A.V. Zayats, and N.I. Zheludev, Active control of surface plasmon–polariton waves. Journal of Optics A: Pure and Applied Optics, 2005. 7(2): p. S85.
3. Anatoly, V.Z. and I.S. Igor, Near-field photonics: surface plasmon polaritons and localized surface plasmons. Journal of Optics A: Pure and Applied Optics, 2003. 5(4): p. S16.
4. Baumberg, J.J., et al., Angle-Resolved Surface-Enhanced Raman Scattering on Metallic Nanostructured Plasmonic Crystals. Nano Letters, 2005. 5(11): p. 2262-2267.
5. Chung, T., et al., Plasmonic Nanostructures for Nano-Scale Bio-Sensing. Sensors, 2011. 11(11): p. 10907-10929.
6. Tan, Y.N., et al., Sensing of Transcription Factor through Controlled-Assembly of Metal Nanoparticles Modified with Segmented DNA Elements. ACS Nano, 2010. 4(9): p. 5101-5110.
7. Larsson, E.M., et al., Sensing Characteristics of NIR Localized Surface Plasmon Resonances in Gold Nanorings for Application as Ultrasensitive Biosensors. Nano Letters, 2007. 7(5): p. 1256-1263.
8. Galush, W.J., et al., A Nanocube Plasmonic Sensor for Molecular Binding on Membrane Surfaces. Nano Letters, 2009. 9(5): p. 2077-2082.
9. Anker, J.N., et al., Biosensing with plasmonic nanosensors. Nat Mater, 2008. 7(6): p. 442-453.
10. Stewart, M.E., et al., Nanostructured Plasmonic Sensors. Chemical Reviews, 2008. 108(2): p. 494-521.
11. McFarland, A.D. and R.P. Van Duyne, Single Silver Nanoparticles as Real-Time Optical Sensors with Zeptomole Sensitivity. Nano Letters, 2003. 3(8): p. 1057-1062.

12. Lee, K.-S. and M.A. El-Sayed, Gold and Silver Nanoparticles in Sensing and Imaging: Sensitivity of Plasmon Response to Size, Shape, and Metal Composition. The Journal of Physical Chemistry B, 2006. 110(39): p. 19220-19225.

13. Sun, Y. and Y. Xia, Increased Sensitivity of Surface Plasmon Resonance of Gold Nanoshells Compared to That of Gold Solid Colloids in Response to Environmental Changes. Analytical Chemistry, 2002. 74(20): p. 5297-5305.

14. Orendorff, C.J., et al., Aspect ratio dependence on surface enhanced Raman scattering using silver and gold nanorod substrates. Physical Chemistry Chemical Physics, 2006. 8(1): p. 165-170.

15. Kretschmann, E., Decay of non radiative surface plasmons into light on rough silver films. Comparison of experimental and theoretical results. Optics Communications, 1972. 6(2): p. 185-187.

16. Jain, P.K., et al., Calculated absorption and scattering properties of gold nanoparticles of different size, shape, and composition: applications in biological imaging and biomedicine. The Journal of Physical Chemistry B, 2006. 110(14): p. 7238-7248.

17. Liz-Marzán, L.M., Tailoring Surface Plasmons through the Morphology and Assembly of Metal Nanoparticles. Langmuir, 2005. 22(1): p. 32-41.

18. Van Duyne, R.P., A.J. Haes, and A.D. McFarland, Nanoparticle optics: fabrication, surface-enhanced spectroscopy, and sensing. 2003: p. 197-207.

19. Juste, J., et al., Gold nanorods: Synthesis, characterization and applications. 36th International Conference on Coordination Chemistry, Merida, Mexico, July 2004, 2005. 249(17-18): p. 1870-1901.

20. Marinakos, S.M., S. Chen, and A. Chilkoti, Plasmonic Detection of a Model Analyte in Serum by a Gold Nanorod Sensor. Analytical Chemistry, 2007. 79(14): p. 5278-5283.

21. Sherry, L.J., et al., Localized Surface Plasmon Resonance Spectroscopy of Single Silver Triangular Nanoprisms. Nano Letters, 2006. 6(9): p. 2060-2065.

22. Bukasov, R., et al., Probing the Plasmonic Near-Field of Gold Nanocrescent Antennas. ACS Nano, 2010. 4(11): p. 6639-6650.

23. Nath, N. and A. Chilkoti, Label-Free Biosensing by Surface Plasmon Resonance of Nanoparticles on Glass: Optimization of Nanoparticle Size. Analytical Chemistry, 2004. 76(18): p. 5370-5378.

24. Kreuzer, M., et al., Colloidal-based localized surface plasmon resonance (LSPR) biosensor for the quantitative determination of stanozolol. Analytical and Bioanalytical Chemistry, 2008. 391(5): p. 1813-1820.

25. Haes, A.J., et al., A Localized Surface Plasmon Resonance Biosensor: First Steps toward an Assay for Alzheimer's Disease. Nano Letters, 2004. 4(6): p. 1029-1034.

26. Huang, C., et al., An on-chip localized surface plasmon resonance-based biosensor for label-free monitoring of antigen-antibody reaction. Microelectron. Eng., 2009. 86(12): p. 2437-2441.

27. Kabashin, A.V., et al., Plasmonic nanorod metamaterials for biosensing. Nat Mater, 2009. 8(11): p. 867-871.

28. Hall, W.P., S.N. Ngatia, and R.P. Van Duyne, LSPR Biosensor Signal Enhancement Using Nanoparticle−Antibody Conjugates. The Journal of Physical Chemistry C, 2011. 115(5): p. 1410-1414.

29. Degiron, A., et al., Optical transmission properties of a single subwavelength aperture in a real metal. Opt. Commun., 2004. 239(1-3): p. 61-66.

30. Stebounova, L., et al., Field localization in very small aperture lasers studied by apertureless near-field microscopy. Appl. Opt., 2006. 45(24): p. 6192-6197.

31. Brolo, A.G., et al., Surface Plasmon Sensor Based on the Enhanced Light Transmission through Arrays of Nanoholes in Gold Films. Langmuir, 2004. 20(12): p. 4813-4815.

32. Ferreira, J., et al., Attomolar Protein Detection Using in-Hole Surface Plasmon Resonance. Journal of the American Chemical Society, 2008. 131(2): p. 436-437.

33. Henzie, J., M.H. Lee, and T.W. Odom, Multiscale patterning of plasmonic metamaterials. Nat Nano, 2007. 2(9): p. 549-554.

34. Hicks, E.M., et al., Plasmonic Properties of Film over Nanowell Surfaces Fabricated by Nanosphere Lithography. The Journal of Physical Chemistry B, 2005. 109(47): p. 22351-22358.

35. Sharma, A. and B. Gupta, Comparison of Performance Parameters of Conventional and Nano-plasmonic Fiber Optic Sensors. Plasmonics, 2007. 2(2): p. 51-54.

36. Verma, R.K. and B.D. Gupta. Surface Plasmon resonance based tapered fiber optic sensor with different taper profiles. in OptoElectronics and Communications Conference, 2009. OECC 2009. 14th. 2009.

37. Wang, S.W., S. Balakrishnan, and P. Georgopoulos, Fast equivalent operational model of tropospheric alkane photochemistry. AIChE Journal, 2005. 51(4): p. 1297-1303.

38. Chang, Y.-J., et al., Nanofiber optic sensor based on the excitation of surface plasmon wave near fiber tip. Journal of Biomedical Optics, 2006. 11(1): p. 014032-014032.

39. Lee, B., S. Roh, and J. Park, Current status of micro- and nano-structured optical fiber sensors. Optical Fiber Technology, 2009. 15(3): p. 209-221.

40. Lyklema, J., et al., Fundamentals of interface and colloid science. 1991, Academic Press: London ;San Diego. p. v.

41. Grzybowski, B.A., et al., Self-assembly: from crystals to cells. Soft Matter, 2009. 5(6): p. 1110-1128.

42. Denkov, N., et al., Mechanism of formation of two-dimensional crystals from latex particles on substrates. Langmuir, 1992. 8(12): p. 3183-3190.

43. Stöber, W., A. Fink, and E. Bohn, Controlled growth of monodisperse silica spheres in the micron size range. Journal of Colloid and Interface Science, 1968. 26(1): p. 62-69.

44. Jiang, P., et al., Single-Crystal Colloidal Multilayers of Controlled Thickness. Chemistry of Materials, 1999. 11(8): p. 2132-2140.

45. Meng, Q.B., et al., Assembly of Highly Ordered Three-Dimensional Porous Structure with Nanocrystalline TiO2 Semiconductors. Chemistry of Materials, 2001. 14(1): p. 83-88.

46. Wong, S., V. Kitaev, and G.A. Ozin, Colloidal Crystal Films: Advances in Universality and Perfection. Journal of the American Chemical Society, 2003. 125(50): p. 15589-15598.

47. Yang, S.M., H. Míguez, and G.A. Ozin, Opal Circuits of Light—Planarized Microphotonic Crystal Chips. Advanced Functional Materials, 2002. 12(6-7): p. 425-431.

48. Vlasov, Y.A., et al., On-chip natural assembly of silicon photonic bandgap crystals. Nature, 2001. 414(6861): p. 289-293.

49. Braun, P.V. and P. Wiltzius, Microporous materials: Electrochemically grown photonic crystals. Nature, 1999. 402(6762): p. 603-604.

50. Calderon, F.L., et al., Direct measurement of colloidal forces. Physical Review Letters, 1994. 72(18): p. 2959-2962.

51. http://en.wikipedia.org/wiki/Computational_electromagnetics.

52. Hao, Y., et al., Fabrication and Magnetic Properties of Ordered Macroporous Nickel Structures. Journal of The Electrochemical Society, 2007. 154(2): p. D65-D69.

53. Chang, S.-H., et al., Optical Fiber-Based Surface-Enhanced Raman Scattering Sensor Using Au Nanovoid Arrays. Plasmonics, 2012. 7(3): p. 501-508.

54. Bartlett, P.N., et al., Highly Ordered Macroporous Gold and Platinum Films Formed by Electrochemical Deposition through Templates Assembled from Submicron Diameter Monodisperse Polystyrene Spheres. Chemistry of Materials, 2002. 14(5): p. 2199-2208.

55. Kelf, T.A., et al., Localized and delocalized plasmons in metallic nanovoids. Physical Review B, 2006. 74(24): p. 245415.

56. Boardman, A., Electromagnetic Surface Modes. 1982: John Wiley and Sons.

57. Bartlett, P.N., et al., Optical properties of nanostructured metal films. Faraday Discussions, 2004. 125: p. 117-132.

58. Teperik, T.V., et al., Strong coupling of light to flat metals via a buried nanovoid lattice: the interplay of localized and free plasmons. Opt. Express, 2006. 14(5): p. 1965-1972.

59. Teperik, T.V., et al., Mie plasmon enhanced diffraction of light from nanoporous metal surfaces. Opt. Express, 2006. 14(25): p. 11964-11971

BIOGRAPHICAL INFORMATION

Jiaqi Wu, he received his B.S. in Materials Science and Engineering from Beijing Institute of Technology in 2010. Since then, he continued to pursue his M.S. in Materials Science and Engineering in the University of Texas at Arlington in Dr. Yaowu Hao's research group. His research projects were related to the optical properties of metal nano-structures and their applications as fiber based plasmonic sensors.